Prevalence of shallow low-frequency earthquakes in the continental crust

***Junichi Nakajima[1] and Akira Hasegawa[2]**

1. School of Science, Tokyo Institute Technology, Japan

2. Graduate School of Science, Tohoku University, Japan

Corresponding author: J. Nakajima (nakajima@geo.titech.ac.jp)

Key points

- Low-frequency earthquakes are more common in the upper crust.
- Earthquakes with predominant low-frequency energy are activated after large crustal earthquakes.
- Differences in the pore-fluid pressure along each fault may be a major cause of the large variation in the observed frequency contents.

Abstract:

Low-frequency earthquakes (LFEs) are categorized as slow earthquakes whose spectral power is concentrated at 1–4 Hz. While the tectonic LFEs along megathrust boundaries occur as shear failure, LFE generation in the continental plate, which is widespread in the lower crust and rarely occurs in the brittle upper crust, is poorly understood due to the diversity of focal mechanism solutions. Here we conduct a systematic survey of LFEs using two metrics (frequency index and peak frequency) that characterize the frequency content of the waveforms, and show that LFEs are prevalent in the upper crust beneath the Japanese Islands, even in non-volcanic regions. Shallow LFEs are most common near tectonic boundaries, and are temporarily activated in the aftershock sequences of large ($M \geq 6.5$) crustal earthquakes. The widespread distribution of shallow LFEs suggests that a lower crustal rheology is not necessary for their genesis. We infer that failure along frictionally weakened faults due to high pore-fluid pressures is a primary control for the enrichment of low-frequency energy. The observed differences in the frequency content are probably due to differences in the pore-fluid pressure along each fault, which influences the rupture velocity and magnitude of the tensile component during shear failure. Our observations may lead to a more unified model of earthquake generation, thereby providing a better understanding of how earthquakes release the stress accumulated in the Earth.

1. Introduction

The recent establishment of a dense seismograph network in Japan has considerably improved earthquake detection capabilities in the region [Okada et al., 2004; Aoi et al., 2020]. The Japan Meteorological Agency (JMA), which routinely determines the locations of earthquakes that have occurred in and around the Japanese Islands, has visually classified earthquakes that possess waveforms with predominant low-frequency energy as low-frequency earthquakes (LFEs) since September 1999. Compared to regular earthquakes, which mainly occur at <10–15 km depth in the continental plate beneath the Japanese Islands [Omuralieva et al., 2012], LFEs are frequently observed at 20–40 km depth (Figure 1) [e.g., Hasegawa and Yamamoto, 1994; Katsumata and Kamaya, 2003; Aso et al., 2013]. LFEs that occur at greater depths than the typical depth limit (brittle–ductile transition depth) for crustal earthquakes (~10–15 km) are often called deep LFEs.

Deep LFEs are primarily observed beneath volcanic regions; however, a number of deep LFEs have also been observed in non-volcanic regions [Aso et al., 2013] (Figure 1). Tectonic LFEs are often interpreted as shear failure along the upper surface of the subducting plate [e.g., Ide et al., 2007; Shelly et al., 2007], whereas the genesis of deep LFEs in the continental crust is poorly understood due to the large range of focal mechanism solutions with varying non-double couple (NDC) components [e.g., Nakamichi et al., 2003; Hensch et al., 2019; Oikawa et al., 2019]. Proposed models for the genesis of deep LFEs include the rapid movement of magma or fluids [Hasegawa and Yamamoto, 1994], failure along a shear-tensile crack [e.g., Wilshire and Kirby, 1989; Nakamichi et al., 2003], magma cooling processes [e.g., Aso and Tsai, 2014], and fluid-pressure transfer related to magmatic processes [e.g., Shapiro et al., 2017].

Shallow LFEs (≤15 km depth) are extremely rare, and are only observed in volcanic regions (Figure 1). However, there have been recent reports of shallow LFEs in the brittle upper crust of non-volcanic regions [e.g., Yoshida et al., 2020; Kosuga, 2019]. The occurrence of shallow LFEs in non-volcanic regions suggests that lower-crustal pressure–temperature conditions are not necessary for LFE generation, which indicates that other factors regulate LFE generation. Therefore, a systematic investigation of the potential prevalence of LFEs in the shallow crust can improve our understanding of the similarities and differences among regular earthquakes, and deep and shallow LFEs, which will provide crucial insights into the physical factors responsible for LFE generation.

We first investigate the frequency content of the seismograms for all crustal earthquakes with JMA magnitude (hereafter referred to as M) of 0–2.5 that occurred beneath the Japanese Islands, and define the LFEs based on their frequency content. We then calculate the stress drops of the

earthquakes occuring in the aftershock areas of ten large crustal earthquakes (M≥6.5) that possessed high LFE activity, and investigate the relationship between the frequency content and stress drop. We highlight that there are temporal variations in the observed LFE activity of each aftershock sequence, and demonstrate that there is a significant increase in shallow LFE activity after large crustal earthquakes (M≥6.5). Finally, we discuss the spatial and temporal characteristics of LFEs, and propose a possible mechanism for LFE generation.

2. Re-definition of LFEs

2-1. Methods and data

We searched for crustal LFEs beneath the Japanese Islands by characterizing their frequency content using two metrics: the frequency index (FI) and peak frequency (f_p). FI is the logarithmic ratio of the velocity spectrum amplitudes of the low- and high-frequency bands, and is defined as $FI = \log_{10}(A_H/A_L)$, where A is the amplitude, and H and L denote the high- and low-frequency bands, respectively [Buurman and West, 2010]. Seismograms with equal amounts of high and low energy have a FI of 0; a negative FI means that the seismogram is dominated by low-frequency energy, whereas a positive FI means that the seismogram is dominated by high-frequency energy. f_p is the frequency with the highest amplitude in the velocity spectrum, which corresponds to the apparent corner frequency of an earthquake, and is influenced by seismic attenuation along the ray path.

We investigated all of the 0≤M≤2.5 earthquakes (N = 984,217) that occurred in the continental plate at 0–35 km depth beneath the Japanese Islands during the 2003–2017 period (Figure 2). We first calculated the spectral amplitudes of the unfiltered velocity waveforms (E–W component) using a 3-s time window that began 0.3 s before the manually picked S-wave onset (Figure 3b). We then estimated the FI values from the amplitudes in the 2–5 and 10–15 Hz frequency bands for A_L and A_H, respectively (Figure 3a), using stations located within a 50-km epicentral distance. We determined f_p from the average amplitude over a 0.66-Hz bandwidth, which was calculated at a 0.33-Hz interval across the analyzed frequency band; the central frequency with the highest amplitude was defined as f_p. We calculated the noise amplitude using a 3-s time window before the P-wave onset, and kept the spectra with signal-to-noise ratios (SNRs) of ≥2 in the 2–15 Hz band. We calculated the station-averaged FI and f_p values for a given earthquake when FI and f_p were obtained at three or more stations for that earthquake.

2-2. Results

Example seismograms for three aftershocks of the 2016 M7.3 Kumamoto Earthquake that were recorded at station N.MSIH located near the epicenter are shown in Figure 3b. The observed FI values for these three aftershocks range from –0.91 to 0.04, even though they possess similar magnitudes (M1.3–1.7). It is obvious that the waveforms enriched in low-frequency energy have smaller FI and f_p values. The smallest FI value (–0.91) is comparable to that for a LFE identified by the JMA (FI = –0.94) (Figure 3c). These observations demonstrate that the FI and f_p values quantify the frequency content of the seismograms.

The station-averaged FI and f_p values for the 397,709 earthquakes whose parameters could be estimated at three or more stations are shown in Figure 4a. FI and f_p are positively correlated, and their distributions include those of the M1 and M2 earthquakes expected from a theoretical ω^2 source model [Brune, 1970], assuming a stress drop ($\Delta\sigma$) of 1 MPa, Q of 200, and travel time of 10 s. The LFEs identified by the JMA (hereafter referred to as JMA LFEs) are shown by the red dots, and are clearly distinguishable from the other earthquakes in the FI–f_p domain (see the histograms on the top and right sides of Figure 4a). The FI and f_p histograms show that FI ≤ -0.75 and $f_p \leq 4$ Hz include 80 and 90% of the JMA LFEs, respectively (Figure 4a). This study re-defined the LFEs using these FI and f_p thresholds (green rectangle in Figure 4a), and 5530 LFEs were defined here.

A magnitude effect is apparent for the FI and f_p values derived from a theoretical ω^2 source model with given typical $\Delta\sigma$, Q, and travel time values (black squares in Figure 4a), but the observed FI and f_p values of earthquakes are less dependent on the earthquake magnitude (Figure 5). The theoretical range of FI and f_p values exhibits a similar trend to the observations (colored squares in Figure 5a) when we calculate the theoretical FI and f_p values using acceptable Q (100, 200, 300, and 400) and $\Delta\sigma$ (0.1, 0.5, 1, 5, and 10 MPa) values, and travel times (5.7, 8.6, and 11.4 s, which correspond to hypocentral distances of 20, 30, and 40 km, respectively, with Vs = 3.5 km/s, where Vs is the S-wave velocity). These results suggest that the variations in seismic attenuation along the ray paths, earthquake $\Delta\sigma$, and observed travel times would mask the magnitude dependence of the FI and f_p values.

Figures 4b and 4c highlight that the frequency metrics for earthquakes at ≤15 km depth are continuously distributed. A local peak at FI = −1.0, which is only visible in the histogram of the entire earthquake catalog (LFEs and regular earthquakes) is apparent due to the occurrence of deep LFEs. This local peak is probably due to considerable attenuation effects associated with the deep LFEs, which possess longer ray paths than those for the earthquakes at <10–15 km depth.

The shallow and deep LFEs detected in this study occurred around volcanic regions (Figures

6a and 6b), which is consistent with the spatial distribution of the JMA LFEs (Figure 1). However, two exceptions, each with significant LFE activity, are evident in two areas across Hokkaido. A comparison of the LFE depth distribution defined in this study and the JMA LFE depth distribution shows that both catalogs are nearly identical at ≥20 km depth; however, our catalog identifies 565 LFEs at ≤10 km depth, whereas the JMA catalog only classifies 40 of these events as JMA LFEs (Figure 6c). This suggests that shallow LFEs may be a relatively common phenomenon, with the vast majority (>90%) being unidentified in the JMA catalog.

2-3. Spatial variations in FI and f_p

We calculated the spatially averaged FI and f_p values of the shallow earthquakes (≤15 km depth) for each 0.2° × 0.2° area with a shift of 0.1° in both longitude and latitude directions to identify any spatial variations in the frequency content of the earthquake waveforms (Figures 7b and c). This calculation was done for all of the earthquakes, regardless of their FI and f_p values. The FI and f_p values both exhibit considerable regional variations; areas with relatively low FI and f_p values, which basically coincide with enhanced LFE activity, likely correspond to major tectonic boundaries (Figure 7a). For example, northern Hokkaido includes the active boundary between the Amurian and Okhotsk plates [Ito et al., 2019], where slow slip is observed along a crustal fault [Ohzono et al., 2015], and the area to the west of Hidaka consists of a deformation zone where the Kuril Forearc has been colliding with the Northeast Japan Arc since ~15 Ma [Kimura, 1994]. A marked low-FI, low-f_p area in the northern part of central Japan corresponds to the Fossa Magna, where pre-Miocene terrains bend in a cusp form [Matsuda, 1978]. A low-f_p area in central Kyushu may be attributable to the Beppu-Shimabara Graben, where marked increases in volcanic, geothermal, and seismic activity are observed [Tada, 1985], even though there is no clear reduction in FI. These observations suggest that the upper crustal tectonic environment controls the regional FI and f_p variations. A possible mechanism for the regional variations in FI and f_p will be discussed in section 6.

We note that both the FI and f_p values would be significantly affected by seismic attenuation along the ray path, even though we observe marked regional variations in FI and f_p. The determined FI and f_p values are potentially underestimated due to attenuation effects since the seismic attenuation along the ray path preferentially decays the high-frequency component of the seismic energy. We therefore attempted to discriminate the path effects from the actual physical variations in the seismic fault by estimating $\Delta\sigma$ for the earthquakes via the S-coda spectral ratio method, which can minimize the seismic attenuation effect. $\Delta\sigma$ is a key parameter for

characterizing the amount of stress released during seismic rupture, and may be related to the frictional strength of the rupture surface (fault).

We focused on 12 specific, non-volcanic areas with major shallow LFE activity to characterize the relationship between the FI and f_p values, and $\Delta\sigma$; two areas in Hokkaido (northern Hokkaido and Hidaka) and ten aftershock areas of large ($M \geq 6.5$) crustal earthquakes (areas with green rectangles in Figure 7d) that occurred at ≤35 km depth during the 2003–2017 period (Table 1).

3. Stress drop estimates

3.1 Methods and data

The S-coda wave amplitudes are insensitive to the source radiation pattern and medium heterogeneity when the lapse time measured from the source origin time is more than twice the direct S-wave travel time [e.g., Sato and Fehler, 1998]. This means that the S-coda waves are not shaped by complex factors, such as the source radiation pattern and medium heterogeneities. These advantages of the S-coda waves have been used to estimate the source parameters from the spectral ratios of S-coda waves [e.g., Mayeda et al., 2007; Somei et al., 2014].

The spectral ratio of the S-coda waves at a common station for two earthquakes has two corners that correspond to the corner frequencies (f_c) of the two earthquakes. The optimum f_c values of each earthquake pair and the level of the spectral ratio were determined via a grid search across the 1–30 Hz frequency band that minimized the misfits between the observed and theoretical spectral ratios.

We selected the $2.0 \leq M \leq 3.5$ earthquakes that occurred at ≤15 km depth in the 12 areas across the Japanese Islands (green areas in Figure 7d). We calculated the spectral amplitudes for the E–W component of the S-coda waves using a 10-s time window that was taken at twice the theoretical S-wave travel time calculated from a 1-D seismic velocity model [Hasegawa et al., 1978]. The noise spectral amplitudes were calculated for the pre-P waves. The frequency range with SNR ≥ 2 was included in the analysis. We limited the earthquake pairs to those with a magnitude difference of ≥0.5 and within a hypocentral distance of 5 km to ensure stable measurements. The average spectral ratio was fit by an ω^2 source model [Brune, 1970] to estimate the f_c values for the earthquake pair when the spectral ratios for that earthquake pair were calculated at five or more common stations; these average f_c values were used in the subsequent analysis. We then calculated $\Delta\sigma$ for the earthquakes using the symmetrical circular crack model of Sato and Hirasawa [1973] and Eshelby's [1957] static solution for the crack, with Vr/Vs = 0.9 and Vs = 3.5 km/s, where Vr is the rupture velocity.

3.2 Results

Figure 8 shows the calculated $\Delta\sigma$ values for 49,476 earthquakes in the 12 areas. Individual $\Delta\sigma$ values range from <0.1 MPa to >10 MPa, with an average $\Delta\sigma$ of 0.65 MPa for all of the earthquakes; the average values among the 12 areas range from 0.35 MPa in northern Hokkaido to 1.38 MPa in western Fukuoka. These values are comparable to the average $\Delta\sigma$ values (0.38–0.67 MPa) for the aftershocks ($Mw \geq 3.2$) of large crustal earthquakes [Somei et al., 2014], but are smaller than the $\Delta\sigma$ estimates (~1–10 MPa) of ordinary crustal earthquakes ($Mw \geq 2.7$) [Oth, 2013]. The spatial $\Delta\sigma$ distributions in this study are similar to the values in the two previous studies, with smaller $\Delta\sigma$ values in northeast Japan and higher $\Delta\sigma$ values in Kyushu [Oth, 2013; Somei et al., 2014]. We consider that the regional variations in $\Delta\sigma$ reflect variations in either the amount of stress release along the seismic faults or the rupture velocity during rupture since the $\Delta\sigma$ values that were estimated via the S-coda spectral ratio method can minimize the effects of the spatial variations in seismic attenuation.

We investigated the relationship between FI and $\Delta\sigma$ for the $2.0 \leq M \leq 2.5$ earthquakes (N = 15345) due to the overlap between the earthquake magnitude ranges used in the FI estimates and those used in the $\Delta\sigma$ estimates, and found a positive correlation between the two parameters (Figure 9). The positive correlation between FI and $\Delta\sigma$ suggests that the FI values reflect the actual amount of stress release along the seismic faults, even though the observed FI values may be affected by seismic attenuation along the ray paths. Figure 9 suggests that FI = –0.50 and –0.25 correspond to $\Delta\sigma$ = ~0.3 and ~1 MPa, respectively.

4. Temporal variations in the frequency content

The re-defined LFEs in this study, which are based on the FI and f_p values ($FI \leq -0.75$ and $f_p \leq 4$ Hz), demonstrated that shallow LFEs are more common than conventionally believed. However, the FI and f_p values possess large regional variations, as shown in Figure 7. Therefore, we introduced independent FI thresholds for each of the ten hypocentral areas and classified the earthquakes with $FI \leq \mu - 3s$ as relative LFEs (r-LFEs), where μ and s are the average and standard deviation of the FI values in a given area, respectively. This strategy means that we can extract the earthquakes that are characterized by relatively predominant low-frequency energy in each area. An investigation of the temporal changes in r-LFE activity for each of the aftershock sequences will provide additional information on the genesis of earthquakes enriched in low-frequency energy.

Figure 10 shows the temporal changes in FI for the shallow earthquakes (≤15 km depth) in the ten hypocentral areas during the analysis period (2003–2017). The r-LFE activity (red dots) is high for the 2008 M7.2 Iwate-Miyagi, 2011 M7.1 Iwaki, and 2016 M7.3 Kumamoto earthquakes. It is evident that the r-LFEs did not occur constantly with time, but were activated after the mainshock in each hypocentral area (green line in Figure 10), with a decay in r-LFE activity over time. Figure 11 shows the cumulative counts of the shallow (≤15 km depth) and deep (>15 km depth) r-LFE activity. There was an increase in shallow r-LFE activity immediately after the mainshock (Figure 11a), in agreement with previous observations where the earthquakes with predominant low-frequency energy occurred in the aftershock sequences [e.g., Obara, 2004; Kosuga, 2011; Kimura and Ukawa, 2018]. However, the deep r-LFE activity is very low and is not enhanced by the mainshock. Approximately constant deep r-LFE activity is only seen for the 2008 Iwate-Miyagi and 2014 Kamishiro sequences, where active volcanoes are included in the aftershock areas (Figure 11c).

Shallow r-LFEs were sometimes triggered by distant earthquakes, and moderate-sized foreshocks and aftershocks. For example, the r-LFE activity in the hypocentral area of the 2004 Chuetsu Earthquake increased moderately after the 2007 Noto-Hanto Earthquake and considerably after the 2011 M9.0 Tohoku-oki Earthquake (Figure 10). For the 2011 Iwaki sequence hypocentral area, the occurrence of an M6.3 earthquake in 2017 appeared to have activated r-LFEs. The r-LFE activity that was observed prior to the mainshocks in the 2011 Iwaki and 2016 Kumamoto sequences (Figure 11b) were in response to the 2011 Tohoku-oki Earthquake and largest (M6.5) foreshock, respectively.

5. The 2016 Kumamoto sequence

5-1. r-LFE activity

Here we focus on the r-LFE activity in the hypocentral area of the 2016 M7.3 Kumamoto Earthquake, where the highest r-LFE activity was observed among the ten aftershock sequences and the r-LFEs occurred at a quasi-constant rate, even before the mainshock (Figures 11a and 12a). Figure 12b shows the r-LFE activity from three days before to ten days after the mainshock. The number of r-LFEs slightly increased after the largest (M6.5) foreshock and was significantly enhanced following the mainshock (M7.3), which occurred 28 h after the M6.5 foreshock. Figure 12c shows that the r-LFE activity following the M6.5 foreshock (yellow symbols) was limited to the vicinity of the foreshock hypocenter, whereas the r-LFE activity expanded across the entire aftershock area after the mainshock (red and white symbols), suggesting that r-LFE activity may

be linked to aftershock activity.

We investigated the temporal variations in the r-LFE activity rates, FI and f_p values, and $\Delta\sigma$ of the earthquakes during the first ten days after the largest foreshock to understand the cause of the temporal changes in r-LFE activity (Figure 13). We calculated the average and standard deviation of the FI and f_p values, and $\Delta\sigma$ for every successive 500 and 50 earthquakes, respectively. The highest r-LFE activity was observed in the first ~6 h after the mainshock, when temporary reductions in FI, f_p, and $\Delta\sigma$ were observed. However, we cannot rule out the possibility that the observed concurrent reductions in FI, f_p, and $\Delta\sigma$ may have been the result of a transient increase in seismic attenuation, even though the S-coda spectral ratio method could minimize the seismic attenuation effect on $\Delta\sigma$ (see section 3-1). Therefore, we evaluated whether seismic attenuation was temporarily enhanced after the mainshock.

5-2. Temporal variations in seismic attenuation

The spectral ratio method is often used to constrain f_c by minimizing the seismic attenuation effects [e.g., Mayeda et al., 2007; Ko et al., 2012]; however, it can be beneficial to directly estimate the difference in seismic attenuation between two earthquakes [e.g., Nakajima and Uchida, 2018; Shiina et al., 2018; Kriegerowski et al., 2019]. Here we estimated the differential attenuation (Δt_{ijm}*) following the method of Nakajima and Uchida (2018), where $\Delta t_{ijm}^* = \Delta t_{im}^* - \Delta t_{jm}^*$, and Δt_{im}^* and Δt_{jm}^* are the seismic attenuation values along ray paths from earthquake i to station m and from earthquake j to station m, respectively. When we correct for the f_c effect on an observed spectrum, the slope of the f_c-corrected spectral ratio for the two earthquakes at a common station is proportional to Δt_{ijm}^* (see Nakajima and Uchida (2018) for further details).

We selected 7990 earthquakes ($2.0 \leq M \leq 3.5$) whose f_c could be estimated via the S-coda spectral ratio method in section 3-1. The spectral amplitudes were calculated using a 3-s window that began at the manually picked S-wave onset, and the noise spectra were calculated using a 3-s window before the P-wave onset. The spectral data with SNR $\geq$ 2 were retained to calculate the f_c-corrected spectral ratios at common stations and determine Δt^* via least-squares fitting of the averaged spectral ratio. This method can resolve the difference in seismic attenuation between two earthquakes when the ray paths from the earthquakes to common stations are almost identical. Therefore, we limited the hypocentral distance between the two earthquakes to $\leq$2 km so that the rays from the two earthquakes sample approximately the same volume. We used stations located within an epicentral distance of $\leq$50 km.

We divided the earthquakes into three periods depending on the occurrence time to resolve the

temporal variations in Δt^*: Period I earthquakes (N = 287) occurred before the M6.5 foreshock on April 14, 2016; Period II earthquakes (N = 562) occurred between the M6.5 foreshock and M7.3 mainshock on April 16, 2016; and Period III earthquakes (N = 4773) occurred after the mainshock. We made earthquake pairs using one from Period I and the other from either Period II or III to estimate the temporal variations in attenuation between either Period I and II or Period I and III. We analyzed 1634 Period I–II earthquake pairs and 8772 Period I–III earthquake pairs.

Figure 13e shows the temporal variations in Δt^* in the source area that were calculated for Periods II and III with respect to Period I. We calculated the average Δt^* and standard deviation values for every 300 successive earthquakes from Periods II and III. The average Δt^* value did not change significantly with time, thereby demonstrating that the enhanced r-LFE activity and temporary reductions in FI, f_p, and $\Delta\sigma$ after the mainshock were not due to increased seismic attenuation in the hypocentral area but rather reflected actual variations in the earthquake source parameters.

5.3 Results for the other areas

Figure 14 shows the temporal variations in the FI values for five hypocentral areas with significant r-LFE activity. The FI values were temporarily reduced after the mainshock and then gradually recovered, with the exception of the 2011 Iwaki Earthquake hypocentral area. Although the temporal changes in the FI values are within one standard deviation and may not be statistically significant, the systematic reduction in FI for at least four of the seismic sequences suggests that the decrease in FI values following the mainshock could reflect time-dependent phenomena in the source area.

Figure 15 shows the r-LFE distribution for the 2008 M7.2 Iwate-Miyagi and 2011 M7.0 Iwaki earthquakes, which are the second and third most active shallow r-LFE sequences, respectively (Figure 11). There was no significant enhancement of shallow r-LFE activity in the areas with high aftershock activity during the 2008 Iwate-Miyagi sequence; however, there was enhanced r-LFE activity near the Quaternary volcanoes to the west of the aftershock area, where separate aftershock activity was also observed. The shallow r-LFE activity was more widespread and decayed with time since the mainshock, whereas the deep r-LFE activity occurred in limited areas and appeared to occur at approximately regular intervals (Figure 11).

The 2011 Iwaki sequence exhibited high r-LFE activity across the entire aftershock area, similar to the 2016 Kumamoto sequence. r-LFEs were activated after the 2011 Tohoku-oki Earthquake, which occurred one month prior to the Iwaki earthquake (Figure 11). Interestingly,

334 the pre-mainshock r-LFEs (yellow circles in Figure 15b) occurred in the northern and southern
335 parts of the aftershock area and were associated with the occurrences of a M6.0 earthquake on
336 March 23 and a M6.1 earthquake on March 19, respectively; these two earthquakes are recognized
337 as earthquakes that were triggered by the Tohoku-oki earthquake. The r-LFE activity was limited
338 to ≤10 km depth, even though numerous aftershocks occurred at ≥15 km depth.
339
340 **6. Discussion**
341 **6.1 A possible mechanism for the reduced FI, f_p, and $\Delta\sigma$ values**
342 The major areas with reduced FI and f_p values correspond to geological and present tectonic
343 boundaries, as described in section 2-3 (Figure 7). We infer that the tectonic boundaries are
344 inherently fractured and permeable due to long-term deformation, and are therefore locally
345 weakened by the large influx of fluids over geologic timescales [Wang et al., 2018; Ito et al.,
346 2019]. This inferred influx of fluids is supported by the presence of low-velocity anomalies in the
347 crust along the tectonic boundaries [e.g., Omuralieva et al., 2012; Zhao et al., 2018].
348 Although $\Delta\sigma$ depends on the focal depth, faulting style (focal mechanism), and the amount of
349 stress released during rupture [Oth, 2013], our systematic analyses of $\Delta\sigma$ for the large number of
350 crustal earthquakes, which possess various faulting styles, would eliminate the effects of the focal
351 depth and faulting style as major causes of the regional variations in $\Delta\sigma$. Therefore, the
352 $\Delta\sigma$ variations probably reflect the variations in the amount of stress released during rupture. Even
353 through our analyses cannot distinguish between the frictional strength of the fault and the rupture
354 velocity as the primary control on the amount of stress release, both parameters can be reduced
355 by elevated pore-fluid pressures [Goertz-Allmann et al., 2011; Urata et al., 2013]. We therefore
356 infer that high pore-fluid pressures would be a candidate for a governing mechanism of the
357 marked decreases in $\Delta\sigma$. The positive correlation between $\Delta\sigma$ and FI (and f_p) suggests that smaller
358 FI and lower f_p values are also caused by high pore pressures.
359
360 **6.2 r-LFE activation after large earthquakes**
361 Geophysical analyses have shown that a marked low-velocity body exists in the middle to lower
362 crust immediately beneath the hypocentral areas of major crustal earthquakes [e.g., Zhao et al.,
363 1996; Hasegawa et al., 2009; Chiarabba et al., 2020] and a high-conductivity area is observed at
364 the deeper extension of each fault system [e.g., Wannamaker et al., 2009], both of which are
365 interpreted as fluid-enriched areas. The accumulation of such fluids below the seismogenic layer,
366 which are presumed to have been originally supplied via dehydration from subducting slabs [e.g.,

Iio et al., 2002; Hasegawa et al., 2005], may gradually migrate into potentially permeable fault zones in the upper crust, with a buildup of pore-fluid pressures occurring along faults that may be sealed via silica precipitation or another means [e.g., Saishu et al., 2017]. A rupture could initiate along the fault when a portion of the fault becomes weaker than the regional stress regime due to the gradual increase in pore-fluid pressure; this process is known as the fault-valve model [Sibson, 1992].

We infer that the activation of shallow r-LFEs following major crustal earthquake sequences can be explained within the framework of fault-valve behavior. The fluids that accumulated along a fault or below the seismogenic zone would be redistributed in the hypocentral area once a large earthquake occurs and breaks the fault valve [e.g., Sibson, 1992; Yoshida and Hasegawa, 2018; Ross et al., 2020]. These processes could cause differential increases in the pore-fluid pressures along hidden faults in the hypocentral area depending on how effectively each fault is sealed, with the aftershocks occurring along these frictionally weakened faults [Miller et al., 2004]. The seismic energy release due to failure along a fault with an elevated pore-fluid pressure that approaches lithostatic pressure is enriched in low-frequency energy probably due to the reduced rupture velocity [e.g., Liu, 2005; Das and Zoback, 2013; Hawthorne et al., 2019]; the earthquakes that radiate this predominant low-frequency energy are recognized as r-LFEs (LFEs). The role of overpressurized fluids in LFE generation is supported by the extremely low $\Delta\sigma$ values for LFEs [e.g., Greenfield et al., 2019; Hensch et al., 2019] and dynamic triggering of shallow LFEs along inland faults via the passage of seismic waves [e.g., Obara, 2012; Chao and Obara, 2016].

The observed concurrent reductions in FI, f_p, and $\Delta\sigma$, and increased r-LFE activity after the Kumamoto earthquake (Figure 13) suggest that the faults in the hypocentral area became temporarily weakened by the redistribution of overpressurized faults. The gradual recoveries in FI, f_p, and $\Delta\sigma$ (Figures 13 and 14) probably reflect a gradual reduction in pore-fluid pressure via fluid diffusion, as observed for earthquakes induced by water injection [e.g., Sumy et al., 2017] or swarm-like natural earthquakes [e.g., Yoshida and Hasegawa, 2018].

6.3 Implications for seismogenesis in the crust

Hayashida et al. [2020] investigated the aftershock focal mechanisms associated with the 2000 M7.3 Western Tottori Earthquake, Japan, using waveform data from an ultra-dense temporary seismic network [Matsumoto et al., 2020], and found that regular earthquakes with a predominant frequency of $\geq$10 Hz contain definite NDC components. This observation suggests that the NDC component is not a unique characteristic for LFEs, but is also relevant to regular earthquakes that

400 are conventionally interpreted as pure shear faulting. The NDC component is interpreted as shear
401 rupture with a tensile component. We hypothesize that the magnitude of the tensile component
402 during failure can be controlled by the pore-fluid pressure level with larger tensile component by
403 higher pore-fluid pressures [e.g., Fischer and Guest, 2011], resulting in the apparent variations in
404 the NDC components of the focal mechanisms, as observed in LFEs [Nakamichi et al., 2003;
405 Hensch et al., 2019; Oikawa et al., 2019].
406 Regular earthquakes primarily occur in the upper crust beneath the Japanese Islands, whereas
407 the majority of the LFEs occur in the lower crust [e.g., Hasegawa and Yamamoto, 1994]. The
408 depth separation of these two earthquake types (Figure 6c) is used as a strong constraint for the
409 LFE generation model, which often requires either the ductile regime or magmatic activity for
410 LFE generation. However, this study demonstrates the prevalence of LFEs (r-LFEs), even in the
411 upper crust. Yoshida et al. (2020) recently revealed that LFEs and regular earthquakes evidently
412 occurred within ~1 km of each other in the upper crust of a non-volcanic area in northern Japan.
413 Furthermore, a rare but not insignificant number of regular earthquakes have occurred in the lower
414 crust beneath the Japanese Islands [e.g., Omuralieva et al., 2012; Nakajima and Uchida, 2018;
415 Katsumata et al., 2019] (see also Figure 15b). These observations suggest that the inherent
416 rheology of the crust is not particularly important in differentiating between the types of
417 earthquake generation, as both LFEs and regular earthquakes can potentially occur throughout
418 the crust.
419 It is considered that the typically ductile lower crust becomes locally and transiently brittle
420 due to elevated pore-fluid pressures [Kohlstedt et al., 1995; White et al., 2011] and high strain
421 rates [Tuffen and Dingwell, 2005]. Brittle lower-crustal earthquakes are frequently observed in
422 continental rifts [e.g., Reyners et al., 2007; Keir et al., 2009], moderately observed in active
423 volcanic centers [e.g., Soosalu et al., 2010; Hotovec-Ellis et al., 2018], and occasionally observed
424 in intracontinental areas [e.g., Leyton et al., 2009; Hong et al., 2020]. These lower-crustal
425 earthquakes often occur in short-lasting swarms and sometimes migrate a few kilometers; they
426 have been interpreted as being triggered by fluid-related phenomena (e.g., magmatic intrusions
427 or fluid-pressure pulses) and transiently induced high strain rates [e.g., Smith et al., 2004; Soosalu
428 et al., 2010; Hotovec-Ellis et al., 2018; Lapins et al., 2020]. Interestingly, the predominant
429 frequencies of lower-crustal M~1 earthquakes vary, ranging from high (≥15 Hz) [Hong et al.,
430 2020] to low (<5 Hz) frequencies [Soosalu et al., 2010]. The earthquakes that dominate the high-
431 frequency signals occur along well-connected permeable networks of preexisting faults [e.g.,
432 Hotovec-Ellis et al., 2018]; such networks may prevent the buildup of pore-fluid pressures to

extremely high values. Conversely, the earthquakes with emergent P and S phases, and predominant low-frequency energy (≤5 Hz) tend to occur in a three-dimensional volume [e.g., Soosalu et al., 2010] that presumably contains poorly defined and less-permeable fractures, thereby promoting pore-fluid pressure buildup to near-lithostatic values. We therefore hypothesize that the magnitude of pore-fluid pressure regulates slip behavior during failure and the increase in pore-fluid pressure to near-lithostatic values dominates the low-frequency energy due to a reduction in the fault strength and/or rupture velocity.

7. Conclusions

We conducted a systematic investigation of crustal earthquakes using large waveform volumes to reveal the spatial and temporal characteristics of LFEs beneath the Japanese Islands. The major findings of this study are summarized as follows.

1. LFEs are more common in the upper crust than conventionally considered.
2. Regional FI and f_p variations are observed among the crustal earthquakes, with the reduced FI and f_p areas corresponding to geological and current active boundaries.
3. Large crustal earthquakes (M≥6.5) often activate earthquakes enriched in low-frequency energy (r-LFEs). Transient reductions in the frictional strength of faults due to the re-distribution of overpressurized fluids in the aftershock area may be a candidate for a governing mechanism of r-LFE generation.

A combined interpretation of our results and reported observations in the literature suggests that the pore-fluid pressure level regulates the amount of low-frequency energy and magnitude of the tensile component of earthquakes during failure along faults, thereby resulting in large variations in the frequency component and focal mechanism solutions of the observed earthquakes. This study suggests that LFEs are not distinct from regular earthquakes, such that the earthquakes containing predominant low-frequency energy are merely identified as LFEs (r-LFEs). Therefore, the discrete classification of earthquakes into LFEs is physically inappropriate, and will either introduce biases or be misleading when investigating the physical factors controlling the frequency content of the observed seismograms, even though LFE classifications are practically useful. Future studies need to quantitatively evaluate the effects of pore-fluid pressures and strain rates on the stress drop and rupture velocity, which will provide crucial constraints on the factors controlling the frequency content of earthquakes.

Acknowledgements

We used the JMA unified hypocenter catalog and waveform data recorded by a nationwide seismograph network in this study. Waveform data can be downloaded at the web page of High Sensitivity Seismograph Network Japan (http://www.hinet.bosai.go.jp). We thank N. Aso for assisting in correcting some of the waveform data. This study was supported by JSPS KAKENHI Grant Numbers JP16H04040, JP16H06475, and JP17K05626.

References

Aoi, S., Y. Asano, T. Kunugi, T. Kimura, K. Uehira, N. Takahashi, H. Ueda, K. Shiomi, T. Matsumoto, and H. Fujiwara (2020), MOWLAS: NIED observation network for earthquake, tsunami and volcano, *Earth, Planets and Space*, *72*, doi:10.1186/s40623-020-01250-x.

Aso, N., and V. C. Tsai (2014), Cooling magma model for deep volcanic long-period earthquakes, *Journal of Geophysical Research: Solid Earth*, *119*, 8442–8456, doi:10.1002/2014JB011180.

Aso, N., K. Ohta, and S. Ide (2013), Tectonic, volcanic, and semi-volcanic deep low-frequency earthquakes in western Japan, *Tectonophysics*, *600*, 27–40, doi:10.1016/j.tecto.2012.12.015.

Brune, J. N. (1970), Tectonic stress and the spectra of seismic shear waves from earthquakes, *Journal of Geophysical Research*, *75*(26), 4997–5009, doi:10.1029/JB075i026p04997.

Buurman, B. H., and M. E. West (2010), Seismic Precursors to Volcanic Explosions During the 2006 Eruption of Augustine Volcano, *In: Power, J.A., Coombs, M.L., Freymueller, J.T. (Eds.), The 2006 Eruption of Augustine Volcano. In: U.S. Geological Survey Professional Paper*, *1769*, 41–57, doi:10.3133/pp17692.

Chao, K., and K. Obara (2016), Triggered tectonic tremor in various types of fault systems of Japan following the 2012 Mw 8.6 Sumatra earthquake, *Journal of Geophysical Research: Solid Earth*, *121*(1), 170–187, doi:10.1002/2015JB012566.

Chiarabba, C., M. Buttinelli, M. Cattaneo, and P. De Gori (2020), Large Earthquakes Driven by Fluid Overpressure: The Apennines Normal Faulting System Case, *Tectonics*, *39*(4), 2–3, doi:10.1029/2019TC006014.

Das, I., and M. D. Zoback (2013), Long-period long-duration seismic events during hydraulic stimulation of shale and tight-gas reservoirs — Part 2: Location and mechanisms, *GEOPHYSICS*, *78*(6), KS109–KS117, doi:10.1190/geo2013-0165.1.

Eshelby, J. D. (1957), The Determination of the Elastic Field of an Ellipsoidal Inclusion, and Related Problems, *Proceedings of the Royal Society of London. Series A*, *241*(1226), 376–396.

Fischer, T., and A. Guest (2011), Shear and tensile earthquakes caused by fluid injection, *Geophysical Research Letters*, *38*(5), L05307, doi:10.1029/2010GL045447.

Goertz-Allmann, B. P., A. Goertz, and S. Wiemer (2011), Stress drop variations of induced earthquakes at the Basel geothermal site, *Geophysical Research Letters*, *38*(9), L09308, doi:10.1029/2011GL047498.

Greenfield, T., D. Keir, J. Kendall, and A. Ayele (2019), Low-frequency earthquakes beneath

506 Tullu Moye volcano, Ethiopia, reveal fluid pulses from shallow magma chamber, *Earth and*
507 *Planetary Science Letters*, *526*, 115782, doi:10.1016/j.epsl.2019.115782.
508 Hasegawa, A., and A. Yamamoto (1994), Deep, low-frequency microearthquakes in or around
509 seismic low-velocity zones beneath active volcanoes in northeastern Japan, *Tectonophysics*,
510 *233*(3–4), 233–252, doi:10.1016/0040-1951(94)90243-7.
511 Hasegawa, A., N. Umino, and A. Takagi (1978), Double-planed structure of the deep seismic
512 zone in the northeastern Japan arc, *Tectonophysics*, *47*(1–2), 43–58, doi:10.1016/0040-
513 1951(78)90150-6.
514 Hasegawa, A., J. Nakajima, N. Umino, and S. Miura (2005), Deep structure of the northeastern
515 Japan arc and its implications for crustal deformation and shallow seismic activity,
516 *Tectonophysics*, *403*(1–4), 59–75, doi:10.1016/j.tecto.2005.03.018.
517 Hasegawa, A., J. Nakajima, N. Uchida, T. Okada, D. Zhao, T. Matsuzawa, and N. Umino (2009),
518 Plate subduction, and generation of earthquakes and magmas in Japan as inferred from
519 seismic observations: An overview, *Gondwana Research*, *16*(3–4), 370–400,
520 doi:10.1016/j.gr.2009.03.007.
521 Hawthorne, J. C., A. M. Thomas, and J.-P. Ampuero (2019), The rupture extent of low frequency
522 earthquakes near Parkfield, CA, *Geophysical Journal International*, *216*(1), 621–639,
523 doi:10.1093/gji/ggy429.
524 Hayashida, Y., S. Matsumoto, Y. Iio, S. Sakai, and A. Kato (2020), Non-Double-Couple
525 Microearthquakes in the Focal Area of the 2000 Western Tottori Earthquake (M 7.3) via
526 Hyperdense Seismic Observations, *Geophysical Research Letters*, *47*(4), 1–9,
527 doi:10.1029/2019GL084841.
528 Hensch, M., T. Dahm, J. Ritter, S. Heimann, B. Schmidt, S. Stange, and K. Lehmann (2019),
529 Deep low-frequency earthquakes reveal ongoing magmatic recharge beneath Laacher See
530 Volcano (Eifel , Germany), 2025–2036, doi:10.1093/gji/ggy532.
531 Hong, T.-K., S. Park, J. Lee, D. Chung, and W. Kim (2020), One-off deep crustal earthquake
532 swarm in a stable intracontinental region of the southwestern Korean Peninsula, *Physics of*
533 *the Earth and Planetary Interiors*, *308*, 106582, doi:10.1016/j.pepi.2020.106582.
534 Hotovec-Ellis, A. J., D. R. Shelly, D. P. Hill, A. M. Pitt, P. B. Dawson, and B. A. Chouet (2018),
535 Deep fluid pathways beneath Mammoth Mountain, California, illuminated by migrating
536 earthquake swarms, *Science Advances*, *4*(8), eaat5258, doi:10.1126/sciadv.aat5258.
537 Ide, S., D. R. Shelly, and G. C. Beroza (2007), Mechanism of deep low frequency earthquakes:
538 Further evidence that deep non-volcanic tremor is generated by shear slip on the plate

539 interface, *Geophysical Research Letters*, *34*(3), 161–177, doi:10.1029/2006GL028890.
540 Iio, Y., T. Sagiya, Y. Kobayashi, and I. Shiozaki (2002), Water-weakened lower crust and its role
541 in the concentrated deformation in the Japanese Islands, *Earth and Planetary Science Letters*,
542 *203*(1), 245–253, doi:10.1016/S0012-821X(02)00879-8.
543 Iio, Y. et al. (2020), Stationarity of aftershock activities of the 2016 Central Tottori Prefecture
544 earthquake revealed by dense seismic observation, *Earth, Planets and Space*, *72*(1),
545 doi:10.1186/s40623-020-01161-x.
546 Ito, C., H. Takahashi, and M. Ohzono (2019), Estimation of convergence boundary location and
547 velocity between tectonic plates in northern Hokkaido inferred by GNSS velocity data,
548 *Earth, Planets and Space*, 71, 86, doi:10.1186/s40623-019-1065-z.
549 Kato, A., S. Sakai, and K. Obara (2011), A normal-faulting seismic sequence triggered by the
550 2011 off the Pacific coast of Tohoku Earthquake: Wholesale stress regime changes in the
551 upper plate, *Earth, Planets and Space*, *63*(7), 745–748, doi:10.5047/eps.2011.06.014.
552 Katsumata, A., and N. Kamaya (2003), Low-frequency continuous tremor around the Moho
553 discontinuity away from volcanoes in the southwest Japan, *Geophysical Research Letters*,
554 *30*(1), 1020, doi:10.1029/2002GL015981.
555 Katsumata, K. et al. (2019), The 2018 Hokkaido Eastern Iburi earthquake (M = 6.7) was triggered
556 by a strike-slip faulting in a stepover segment: insights from the aftershock distribution and
557 the focal mechanism solution of the main shock, *Earth, Planets and Space*, *71*, 53,
558 doi:10.1186/s40623-019-1032-8.
559 Keir, D., I. D. Bastow, K. A. Whaler, E. Daly, D. G. Cornwell, and S. Hautot (2009), Lower
560 crustal earthquakes near the Ethiopian rift induced by magmatic processes, *Geochemistry,*
561 *Geophysics, Geosystems*, *10*(6), doi:10.1029/2009GC002382.
562 Kimura, G. (1994), The latest Cretaceous-Early Paleogene rapid growth of accretionary complex
563 and exhumation of high pressure series metamorphic rocks in northwestern Pacific margin,
564 *Journal of Geophysical Research: Solid Earth*, *99*(B11), 22147–22164,
565 doi:10.1029/94JB00959.
566 Kimura, M., and M. Ukawa (2018), Characteristic low frequency aftershocks in the 2016
567 Kumamoo earthquake (in Japanese with English abstract), Proceedings of the Institute of
568 Natural Sciences, Nihon University, 53, 17–28.
569 Ko, Y. T., B. Y. Kuo, and S. H. Hung (2012), Robust determination of earthquake source
570 parameters and mantle attenuation, *Journal of Geophysical Research: Solid Earth*, *117*(4),
571 161–177, doi:10.1029/2011JB008759.

572 Kohlstedt, D. L., B. Evans, and S. J. Mackwell (1995), Strength of the lithosphere: Constraints
573 imposed by laboratory experiments, *Journal of Geophysical Research: Solid Earth*, *100*(B9),
574 17587–17602, doi:10.1029/95JB01460.
575 Kosuga, M. (2019), Low frequency earthquakes among the aftershocks of Iwate-Miyagi Nairiku
576 earthquake in 2008 : Masahiro KOSUGA and the Group for the aftershock observations of
577 the Iwate-Miyagi Nairiku Earthquake in 2008, Tohoku Research Group for Natural Disaster
578 Science, 47, 1–6.
579 Kosuga, M. (2019), Low-frequency earthquakes in the shallow crust, Tohoku Research Group for
580 Natural Disaster Science, 55, 173–178.
581 Kriegerowski, M., S. Cesca, M. Ohrnberger, T. Dahm, and F. Krüger (2019), Event couple
582 spectral ratio Q method for earthquake clusters: Application to northwest Bohemia, *Solid*
583 *Earth*, *10*(1), 317–328, doi:10.5194/se-10-317-2019.
584 Lapins, S., J. M. Kendall, A. Ayele, M. Wilks, A. Nowacki, and K. V. Cashman (2020), Lower-
585 Crustal Seismicity on the Eastern Border Faults of the Main Ethiopian Rift, *Journal of*
586 *Geophysical Research: Solid Earth*, *125*(8), 1–11, doi:10.1029/2020JB020030.
587 Leyton, F., J. Ruiz, J. Campos, and E. Kausel (2009), Intraplate and interplate earthquakes in
588 Chilean subduction zone: A theoretical and observational comparison, *Physics of the Earth*
589 *and Planetary Interiors*, *175*(1–2), 37–46, doi:10.1016/j.pepi.2008.03.017.
590 Liu, Y., and J.R. Rice (2005), Aseismic slip transients emerge spontaneously in three-dimensional
591 rate and state modeling of subduction earthquake sequences, *Journal of Geophysical*
592 *Research*, *110*(B8), B08307, doi:10.1029/2004JB003424.
593 Matsuda, T. (1978), Collision of the izu-bonin arc with central honshu: cenozoic tectonics of the
594 fossa magna, Japan, *Journal of Physics of the Earth*, *26*, S409–S420,
595 doi:10.4294/jpe1952.26.Supplement_S409.
596 Matsumoto, S., Y. Iio, S. Sakai, and A. Kato (2020), Inelastic strain in the hypocentral region of
597 the 2000 Western Tottori earthquake (M7.3) inferred from aftershock seismic moment
598 tensors, *Earth, Planets and Space*, *72*(1), doi:10.1186/s40623-020-01186-2.
599 Mayeda, K., L. Malagnini, and W. R. Walter (2007), A new spectral ratio method using narrow
600 band coda envelopes: Evidence for non-self-similarity in the Hector Mine sequence,
601 *Geophysical Research Letters*, *34*(11), 161–177, doi:10.1029/2007GL030041.
602 Miller, S. a, C. Collettini, L. Chiaraluce, M. Cocco, M. Barchi, and B. J. P. Kaus (2004),
603 Aftershocks driven by a high-pressure CO2 source at depth., *Nature*, *427*(6976), 724–727,
604 doi:10.1038/nature02251.

605 Mitsuoka, A. et al. (2020), Spatiotemporal Change in the Stress State Around the Hypocentral
606 Area of the 2016 Kumamoto Earthquake Sequence, *Journal of Geophysical Research: Solid*
607 *Earth*, *125*(9), 1–21, doi:10.1029/2019JB018515.
608 Nakajima, J., and N. Uchida (2018), Repeated drainage from megathrusts during episodic slow
609 slip, *Nature Geoscience*, *11*, 351–356, doi:10.1038/s41561-018-0090-z.
610 Nakamichi, H., H. Hamaguchi, S. Tanaka, S. Ueki, T. Nishimura, and A. Hasegawa (2003),
611 Source mechanisms of deep and intermediate-depth low-frequency earthquakes beneath
612 Iwate volcano, northeastern Japan, *Geophysical Journal International*, *154*(3), 811–828,
613 doi:10.1046/j.1365-246X.2003.01991.x.
614 Obara, K. (2004), Shallow low-frequency earthquakes in the sequence of aftershock activity of
615 Mid Niigata prefecture earthquake on October 23, 2004 (in Japanese), Report of the
616 coodination committee for earthquake prediction,73, 371.
617 Obara, K. (2012), New detection of tremor triggered in Hokkaido, northern Japan by the 2004
618 Sumatra-Andaman earthquake, *Geophysical Research Letters*, *39*(20), 161–177,
619 doi:10.1029/2012GL053339.
620 Ohzono, M., H. Takahashi, and M. Ichiyanagi (2015), An intraplate slow earthquake observed by
621 a dense GPS network in Hokkaido, northernmost Japan, *Geophysical Journal International*,
622 *200*(1), 144–148, doi:10.1093/gji/ggu380.
623 Oikawa, G., N. Aso, and J. Nakajima (2019), Focal Mechanisms of Deep Low-Frequency
624 Earthquakes Beneath Zao Volcano, Northeast Japan, and Relationship to the 2011 Tohoku
625 Earthquake, *Geophysical Research Letters*, *46*(13), 7361–7370,
626 doi:10.1029/2019GL082577.
627 Okada, T., N. Umino, and T. Matsuzawa, et al. (2005), Aftershock distribution and 3D seismic
628 velocity structure in and around the focal area of the 2004 mid Niigata prefecture earthquake
629 obtained by applying double-difference tomography to dense temporary seismic network,
630 *Earth Planets Space*, *57*, 435–440.
631 Okada, T., N. Umino, and A. Hasegawa (2012), Hypocenter distribution and heterogeneous
632 seismic velocity structure in and around the focal area of the 2008 Iwate-Miyagi Nairiku
633 Earthquake, NE Japan—Possible seismological evidence for a fluid driven compressional
634 inversion earthquake, *Earth, Planets and Space*, *64*(9), 717–728,
635 doi:10.5047/eps.2012.03.005.
636 Okada, Y., K. Kasahara, S. Hori, K. Obara, S. Sekiguchi, H. Fujiwara, and A. Yamamoto (2004),
637 Recent progress of seismic observation networks in Japan —Hi-net, F-net, K-NET and KiK-

638 net—, *Earth, Planets and Space*, *56*(8), xv–xxviii, doi:10.1186/BF03353076.
639 Omuralieva, A. M., A. Hasegawa, T. Matsuzawa, J. Nakajima, and T. Okada (2012), Lateral
640 variation of the cutoff depth of shallow earthquakes beneath the Japan Islands and its
641 implications for seismogenesis, *Tectonophysics*, *518–521*(1–4), 93–105,
642 doi:10.1016/j.tecto.2011.11.013.
643 Oth, A. (2013), On the characteristics of earthquake stress release variations in Japan, *Earth and*
644 *Planetary Science Letters*, *377–378*, 132–141, doi:10.1016/j.epsl.2013.06.037.
645 Reyners, M., D. Eberhart-Phillips, and G. Stuart (2007), The role of fluids in lower-crustal
646 earthquakes near continental rifts., *Nature*, *446*(7139), 1075–1078,
647 doi:10.1038/nature05743.
648 Ross, Z. E., E. S. Cochran, D. T. Trugman, and J. D. Smith (2020), 3D fault architecture controls
649 the dynamism of earthquake swarms, *Science*, *368*, 1357–1361,
650 doi:10.1126/science.abb0779.
651 Saishu, H., A. Okamoto, and M. Otsubo (2017), Silica precipitation potentially controls
652 earthquake recurrence in seismogenic zones, *Scientific Reports*, *7*(1), 13337,
653 doi:10.1038/s41598-017-13597-5.
654 Sakai, S., A. Kato, T. Iidaka, T. Iwasaki, E. Kurashimo, T. Igarashi, N. Hirata, and T. Kanazawa
655 (2008), Highly resolved distribution of aftershocks of the 2007 Noto Hanto earthquake by a
656 dense seismic observation, *Earth, Planets and Space*, *60*(2), 83–88.
657 Sato, T., and T. Hirasawa (1973), Body wave spectra from propagating shear cracks., *Journal of*
658 *Physics of the Earth*, *21*(1–4), 415–431, doi:10.4294/jpe1952.21.415.
659 Shapiro, N. M., D. V. Droznin, S. Y. Droznina, S. L. Senyukov, A. A. Gusev, and E. I. Gordeev
660 (2017), Deep and shallow long-period volcanic seismicity linked by fluid-pressure transfer,
661 *Nature Geoscience*, *10*(6), 442–445, doi:10.1038/ngeo2952.
662 Shelly, D. R., G. C. Beroza, and S. Ide (2007), Non-volcanic tremor and low-frequency
663 earthquake swarms., *Nature*, *446*(7133), 305–307, doi:10.1038/nature05666.
664 Shiina, T., J. Nakajima, and T. Matsuzawa (2018), P-wave attenuation in the Pacific slab beneath
665 northeastern Japan revealed by the spectral ratio of intraslab earthquakes, *Earth and*
666 *Planetary Science Letters*, *489*, 37–48, doi:10.1016/j.epsl.2018.02.032.
667 Shimizu, H. et al. (2006), Aftershock seismicity and fault structure of the 2005 West Off Fukuoka
668 Prefecture Earthquake (MJMA7.0) derived from urgent joint observations, *Earth, Planets*
669 *and Space*, *58*(12), 1599–1604, doi:10.1186/BF03352668.
670 Shimojo, K., B. Enescu, Y. Yagi, and T. Takeda (2014), Fluid-driven seismicity activation in

671 northern Nagano region after the 2011 M9.0 Tohoku-oki earthquake, *Geophysical Research*
672 *Letters*, *41*(21), 7524–7531, doi:10.1002/2014GL061763.
673 Shinohara, M. et al. (2008), Precise aftershock distribution of the 2007 Chuetsu-oki Earthquake
674 obtained by using an ocean bottom seismometer network, *Earth, Planets and Space*, *60*(11),
675 1121–1126, doi:10.1186/BF03353147.
676 Sibson, R. H. (1992), Fault-valve behavior and the hydrostatic-lithostatic fluid pressure interface,
677 *Earth-Science Reviews*, *32*(1–2), 141–144, doi:10.1016/0012-8252(92)90019-P.
678 Smith, K. D., D. Von Seggern, G. Blewitt, L. Preston, J. G. Anderson, B. P. Wernicke, and J. L.
679 Davis (2004), Evidence for deep magma injection beneath Lake Tahoe, Nevada-California,
680 *Science*, *305*(5688), 1277–1280, doi:10.1126/science.1101304.
681 Somei, K., K. Asano, T. Iwata, and K. Miyakoshi (2014), Source Scaling of Inland Crustal
682 Earthquake Sequences in Japan Using the S-Wave Coda Spectral Ratio Method, *Pure and*
683 *Applied Geophysics*, *171*(10), 2747–2766, doi:10.1007/s00024-014-0774-2.
684 Soosalu, H., J. Key, R. S. White, C. Knox, P. Einarsson, and S. S. Jakobsdóttir (2010), Lower-
685 crustal earthquakes caused by magma movement beneath Askja volcano on the north
686 Iceland rift, *Bulletin of Volcanology*, *72*(1), 55–62, doi:10.1007/s00445-009-0297-3.
687 Sumy, D. F., C. J. Neighbors, E. S. Cochran, and K. M. Keranen (2017), Low stress drops
688 observed for aftershocks of the 2011 Mw 5.7 Prague, Oklahoma, earthquake, *Journal of*
689 *Geophysical Research: Solid Earth*, *122*(5), 3813–3834, doi:10.1002/2016JB013153.
690 Tada, T. (1985), Spreading of the Okinawa Trough and Its Relation to the Crustal Deformation
691 in the Kyushu (In Japnese with English abstract), *Zisin*, *38*(1), 1–12,
692 doi:10.4294/zisin1948.38.1_1.
693 Tuffen, H., and D. Dingwell (2005), Fault textures in volcanic conduits: evidence for seismic
694 trigger mechanisms during silicic eruptions, *Bulletin of Volcanology*, *67*(4), 370–387,
695 doi:10.1007/s00445-004-0383-5.
696 Urata, Y., K. Kuge, and Y. Kase (2013), Suppression of slip and rupture velocity increased by
697 thermal pressurization: Effect of dilatancy, *Journal of Geophysical Research: Solid Earth*,
698 *118*(11), 5827–5837, doi:10.1002/2013JB010640.
699 Wang, H., D. Zhao, Z. Huang, M. Xu, L. Wang, Y. Nishizono, and H. Inakura (2018), Crustal
700 tomography of the 2016 Kumamoto earthquake area in West Japan using P and PmP data,
701 *Geophysical Journal International*, 214, 1151–1163, doi:10.1093/gji/ggy177.
702 Wannamaker, P. E., T. G. Caldwell, G. R. Jiracek, V. Maris, G. J. Hill, Y. Ogawa, H. M. Bibby,
703 S. L. Bennie, and W. Heise (2009), Fluid and deformation regime of an advancing

704 subduction system at Marlborough, New Zealand, *Nature*, *460*(7256), 733–736,
705 doi:10.1038/nature08204.
706 White, R. S., J. Drew, H. R. Martens, J. Key, H. Soosalu, and S. S. Jakobsdóttir (2011), Dynamics
707 of dyke intrusion in the mid-crust of Iceland, *Earth and Planetary Science Letters*, *304*(3–
708 4), 300–312, doi:10.1016/j.epsl.2011.02.038.
709 Wilshire, H. G., and S. H. Kirby (1989), Dikes, joints, and faults in the upper mantle,
710 *Tectonophysics*, *161*(1–2), 23–31, doi:10.1016/0040-1951(89)90298-9.
711 Yoshida, K., and A. Hasegawa (2018), Hypocenter Migration and Seismicity Pattern Change in
712 the Yamagata-Fukushima Border, NE Japan, Caused by Fluid Movement and Pore Pressure
713 Variation, *Journal of Geophysical Research: Solid Earth*, *123*(6), 5000–5017,
714 doi:10.1029/2018JB015468.
715 Yoshida, K., A. Hasegawa, S. Noguchi, and K. Kasahara (2020), Low-frequency earthquakes
716 observed in close vicinity of repeating earthquakes in the brittle upper crust of Hakodate,
717 Hokkaido, northern Japan, *Geophysical Journal International*, *223*(3), 1724–1740,
718 doi:10.1093/gji/ggaa418.
719 Zhao, D., H. Kanamori, H. Negishi, and D. Wiens (1996), Tomography of the source area of the
720 1995 Kobe earthquake: Evidence for fluids at the hypocenter?, *Science*, *274*(5294), 1891–
721 1894, doi:10.1126/science.274.5294.1891.
722 Zhao, D., K. Yamashita, and G. Toyokuni (2018), Tomography of the 2016 Kumamoto
723 earthquake area and the Beppu-Shimabara graben, *Scientific Reports*, *8*(1), 1–11,
724 doi:10.1038/s41598-018-33805-0.
725

726 **Table 1. Summary of parameters for M≥6.5 earthquakes**

727

Area	Earthquake	Date	M	FI	$\log_{10}$(fp), Hz	$\log_{10}(\Delta\sigma)$, Pa	N of shallow r-LFEs
1	Iwate-Miyagi[1)]	2008/6/14	7.2	–0.08±0.14	0.90±0.16	6.08±0.47	135
2	Iwaki[2)]	2011/4/11	7.0	–0.10±0.14	0.87±0.17	6.06±0.22	232
3	Chuetsu[3)]	2004/10/23	6.8	–0.11±0.15	0.93±0.16	6.11±0.40	14
4	Chuetsu-oki[4)]	2007/7/16	6.8	–0.29±0.17	0.73±0.11	5.82±0.34	1
5	N. Nagano[5)]	2011/3/12	6.7	–0.27±0.13	0.79±0.14	5.61±0.38	41
6	Kamishiro[6)]	2014/11/22	6.7	–0.34±0.15	0.74±0.12	5.80±0.39	53
7	Noto-Hanto[7)]	2007/3/25	6.9	–0.16±0.13	0.78±0.14	6.07±0.44	60
8	C. Tottori[8)]	2016/10/21	6.6	–0.16±0.12	0.91±0.23	6.02±0.42	54
9	W. Fukuoka[9)]	2005/3/20	7.0	–0.14±0.15	0.82±0.20	6.20±0.38	26
10	Kumamoto[10)]	2016/4/16	7.3	–0.12±0.15	0.82±0.12	6.10±0.41	228

728 1) Okada et al. [2012], 2) Kato et al. [2011], 3) Okada et al. [2005], 4) Shinohara et al. [2008] 5) Shimojo
729 et al. [2014], 6) 7) Sakai et al. [2008], 8) Iio et al. [2020], 9) Shimizu et al. [2006] 10) Mitsuoka et al. [2020]
730
731

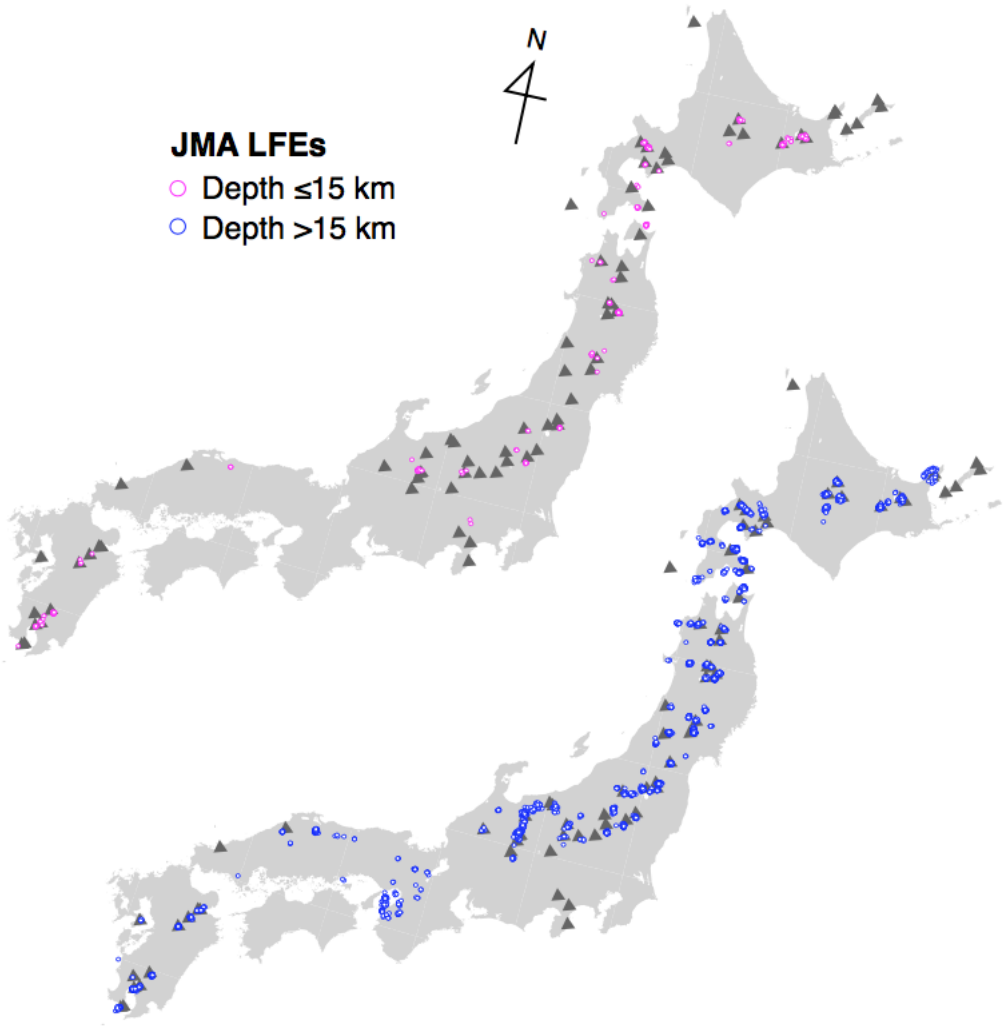

Figure 1. Low-frequency earthquake (LFE) distribution reported in the JMA catalog for the 2003–2017 period. The upper and lower panels show LFEs at ≤15 km and >15 km depth, respectively. The gray triangles denote active volcanoes.

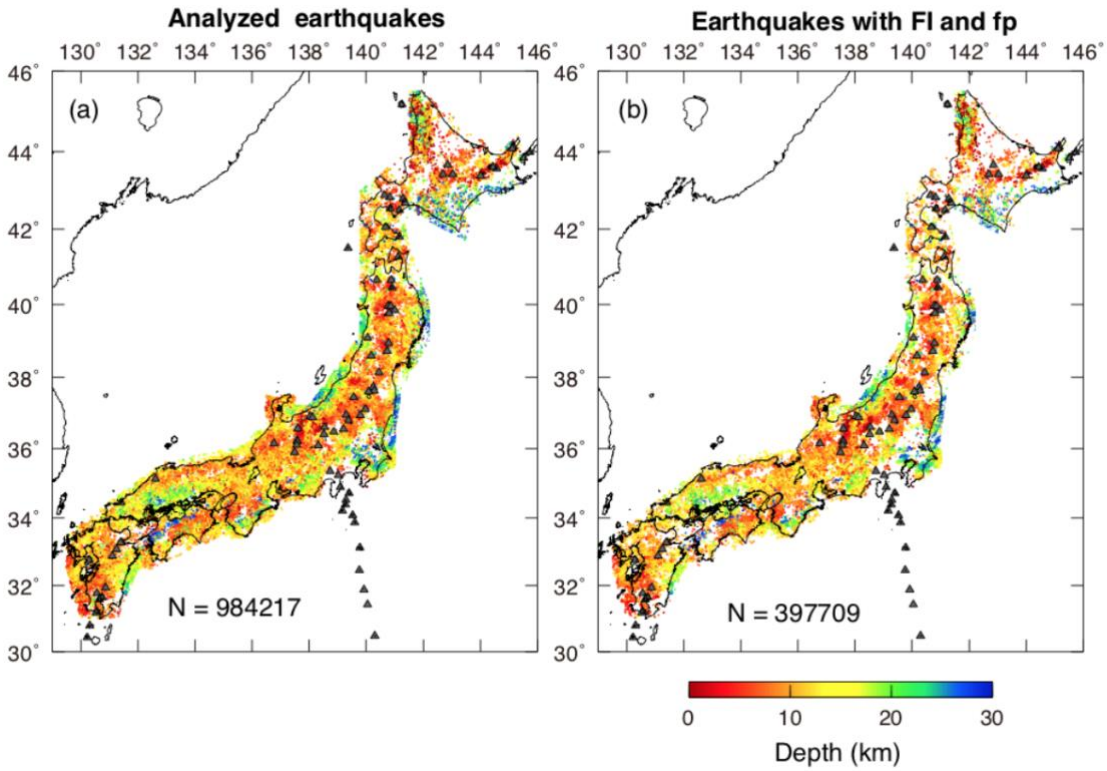

Figure 2. (a) Analyzed earthquake distribution. The hypocenters are color-coded by focal depth. The gray triangles denote active volcanoes. (b) Earthquake distribution for the events whose FI and f_p values have been estimated at three or more stations.

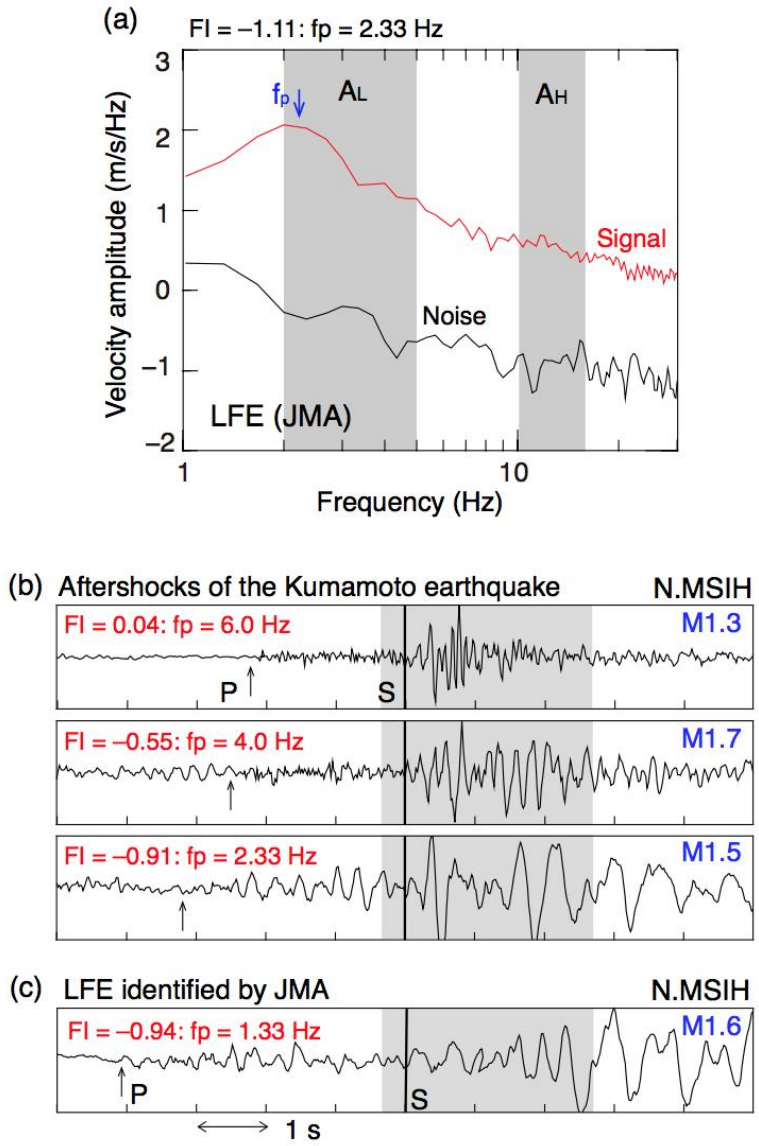

Figure 3. (a) S-wave (red) and noise (black) frequency spectra for a given LFE. The frequency ranges used to determine A_H and A_L for the FI calculation are shown by the gray bands. (b) Example waveforms for three aftershocks of the 2016 Kumamoto Earthquake (M7.3) that were recorded at station N.NSIH. The waveforms are normalized by the maximum amplitudes of each trace and aligned on the S-wave onset. The total waveform length is 10 s. The gray bands represent the 3-s time windows used to calculate the signal spectra. The P-wave arrivals are indicated by the arrows. The FI and f_p values that have been calculated for each earthquake are shown in red, and the magnitudes are indicated in blue. (c) Example LFE waveform recorded at N.MSIH. The other symbols are the same as those in (b).

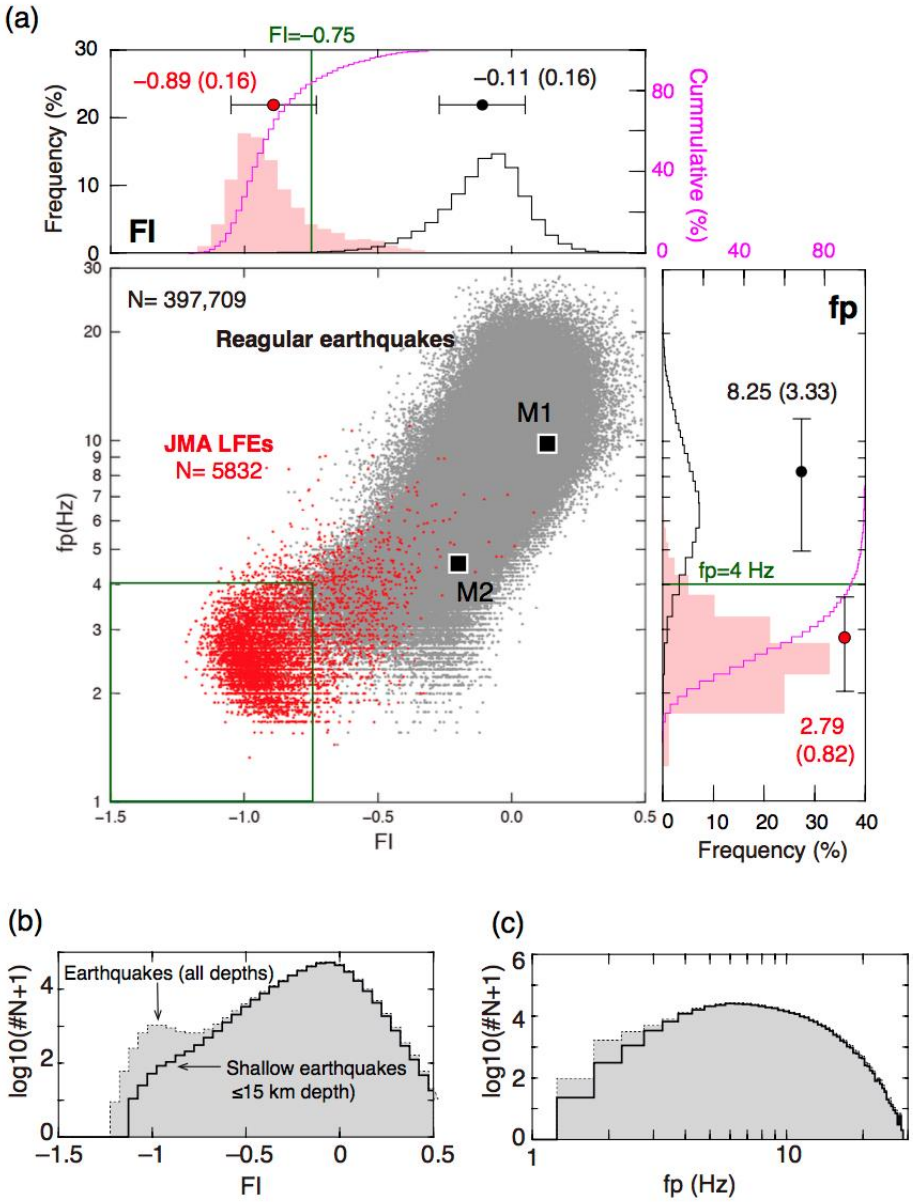

753

754 **Figure 4.** (a) FI and f_p plots for the regular earthquakes (gray) and LFEs (red) that were detected
755 by the JMA. The black squares represent the theoretical values for M1 and M2 earthquakes that
756 were calculated using the ω^2 source model [Brune, 1970] with $\Delta\sigma$ = 1 MPa, Q = 200, and a travel
757 time of 10 s. The green rectangle shows the study domain, which primarily contains earthquakes
758 that are defined as LFEs. The FI and f_p histograms and cumulative curves for regular earthquakes
759 (black) and JMA LFEs (red and magenta) are shown in the upper and right panels, respectively,
760 with the average and standard deviation (in parentheses) values provided. (b) FI frequency
761 histograms for earthquakes in the 0–35 km (gray) and 0–15 km (black) depth intervals. (c) f_p
762 frequency histograms for earthquakes in the 0–35 km (gray) and 0–15 km (black) depth intervals.

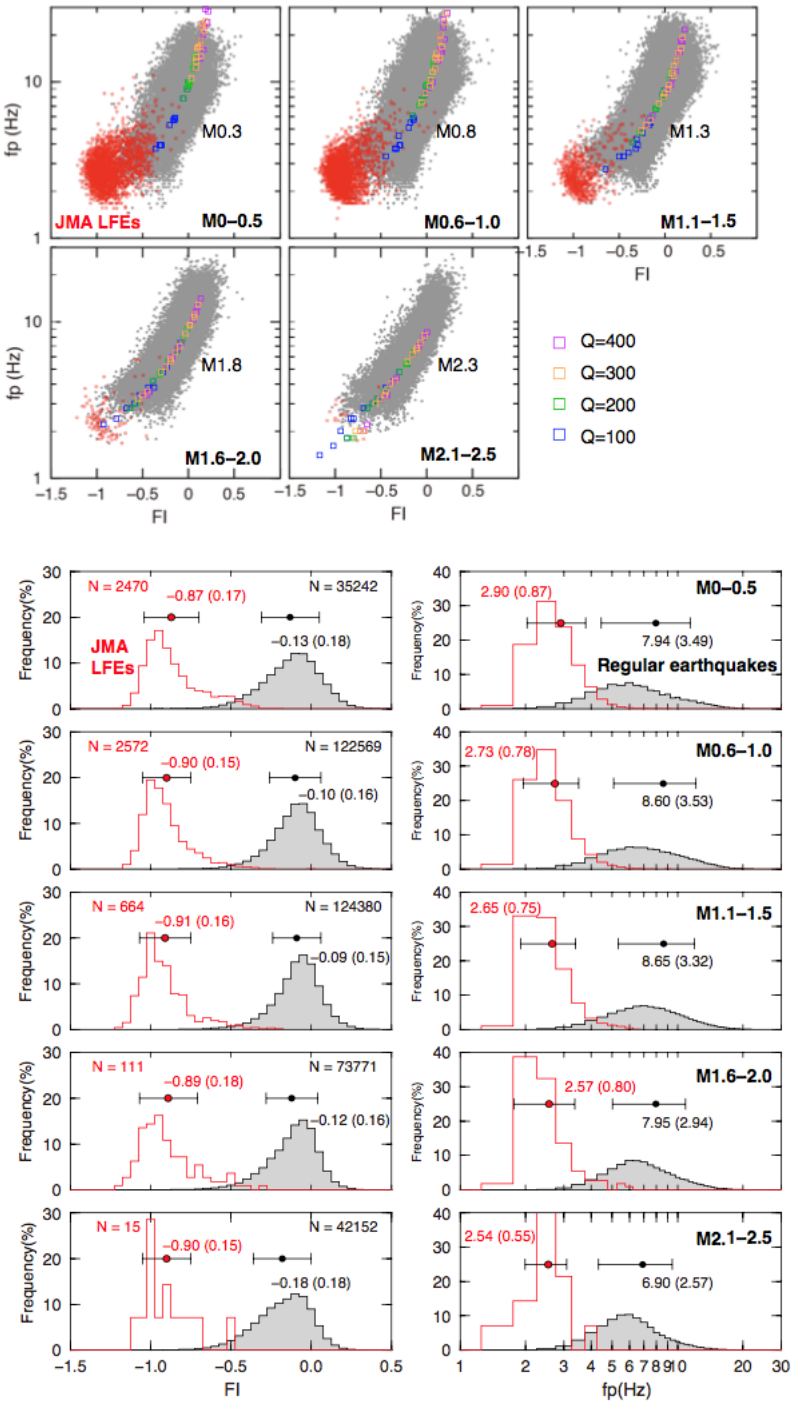

Figure 5. (a) FI and f_p plots for regular earthquakes (gray) and JMA LFEs (red) over five magnitude ranges. The colored squares show the theoretically expected range of FI and f_p values for an earthquake calculated using acceptable ranges of Q (100, 200, 300, and 400) and $\Delta\sigma$ (0.1, 0.5, 1, 5, and 10 MPa), and 5.7, 8.6, and 11.4 s travel times (based on hypocentral distances of 20, 30, and 40 km and Vs = 3.5 km/s, respectively). (b) (left) FI and (right) f_p frequency

histograms for the five magnitude ranges. The other symbols are the same as those in Figure 1c.

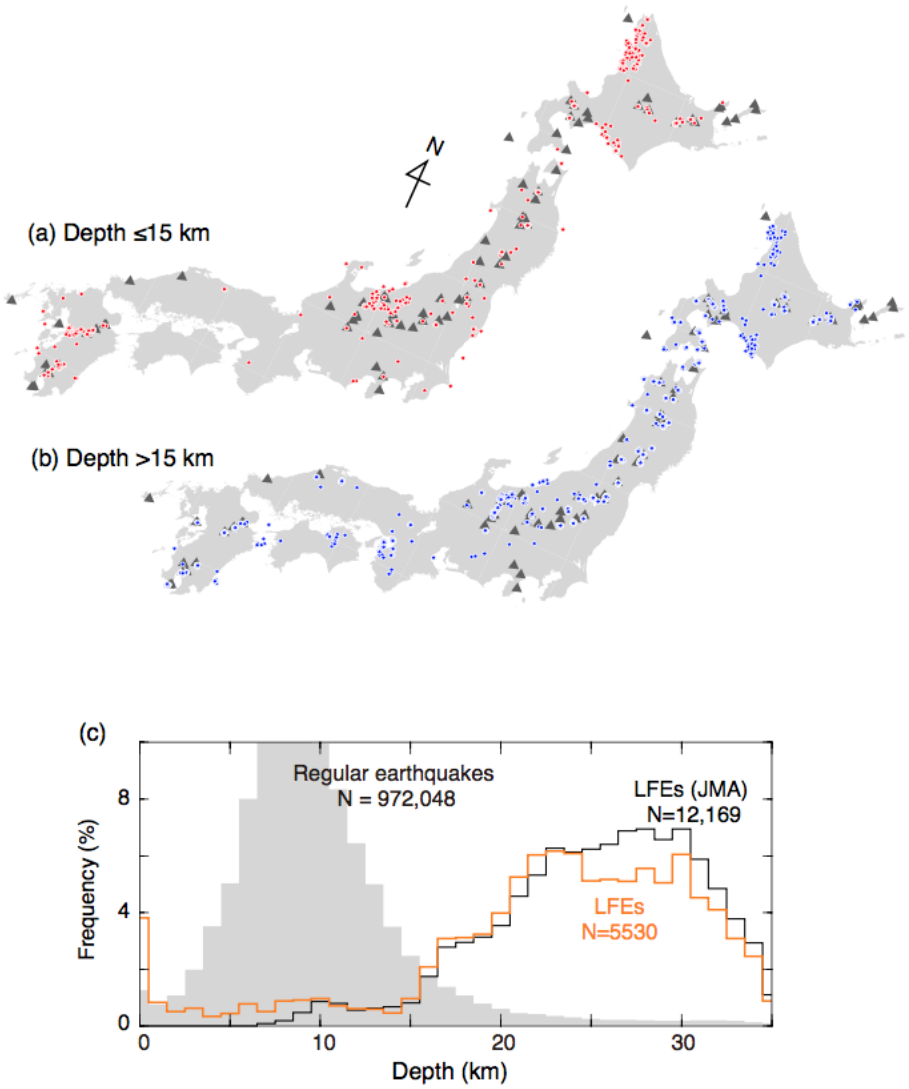

Figure 6. Depth distributions of the (a) shallow (≤15 km depth) and (b) deep LFEs (>15 km depth) defined in this study. The gray triangles denote active volcanoes. (c) Depth distributions of the JMA LFEs (black), LFEs defined in this study (orange), and regular earthquakes (gray shading).

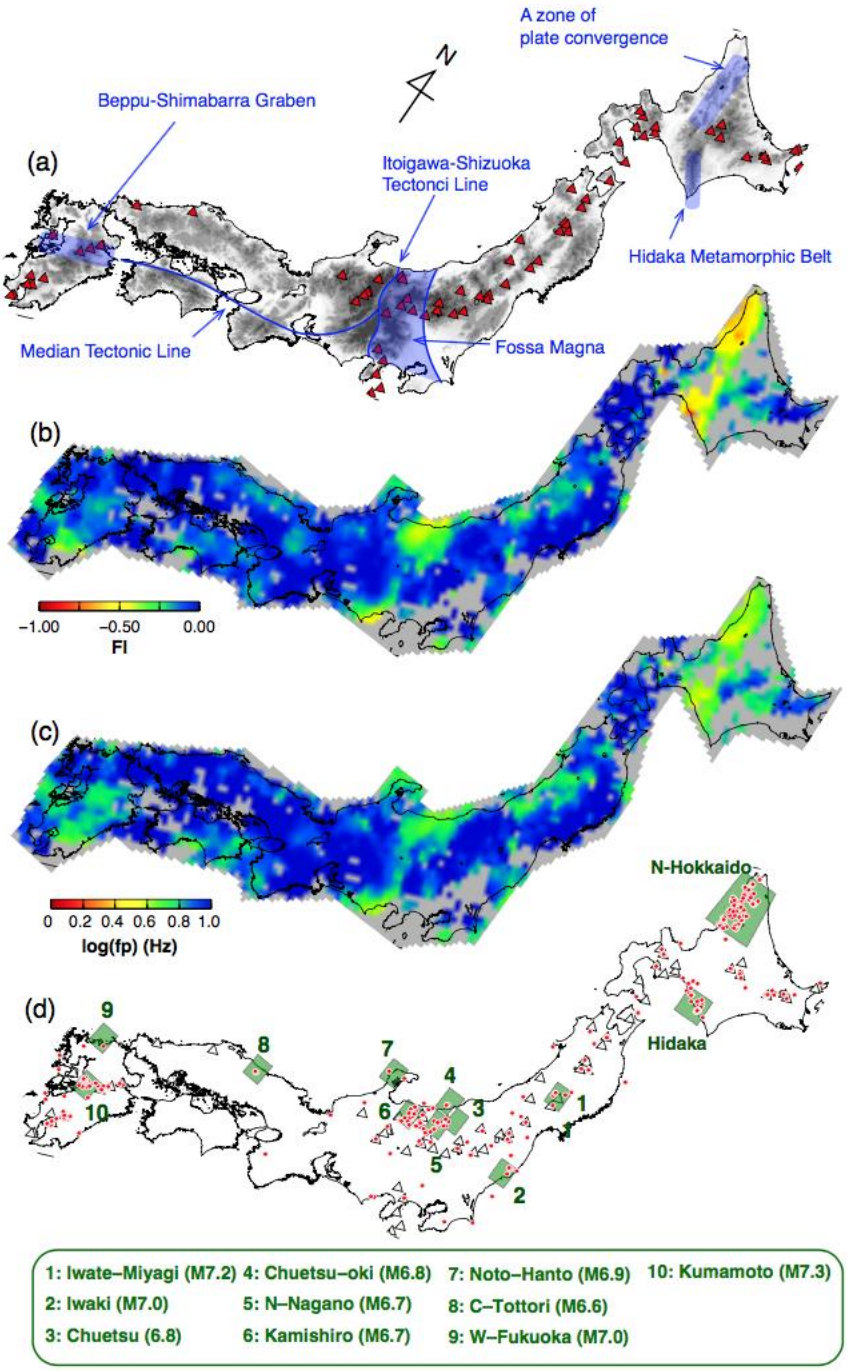

Figure 7. (a) Distributions of the volcanoes (red), topography (gray), and major tectonic boundaries (blue) across the Japanese Islands. (b) FI and (c) f_p maps for the shallow crustal earthquakes (≤15 km depth). (d) Shallow LFE distribution for the 2003–2017 period. The two areas in Hokkaido and ten hypocentral area of large (M≥6.5) crustal earthquakes that were analyzed in this study are highlighted by the green rectangles.

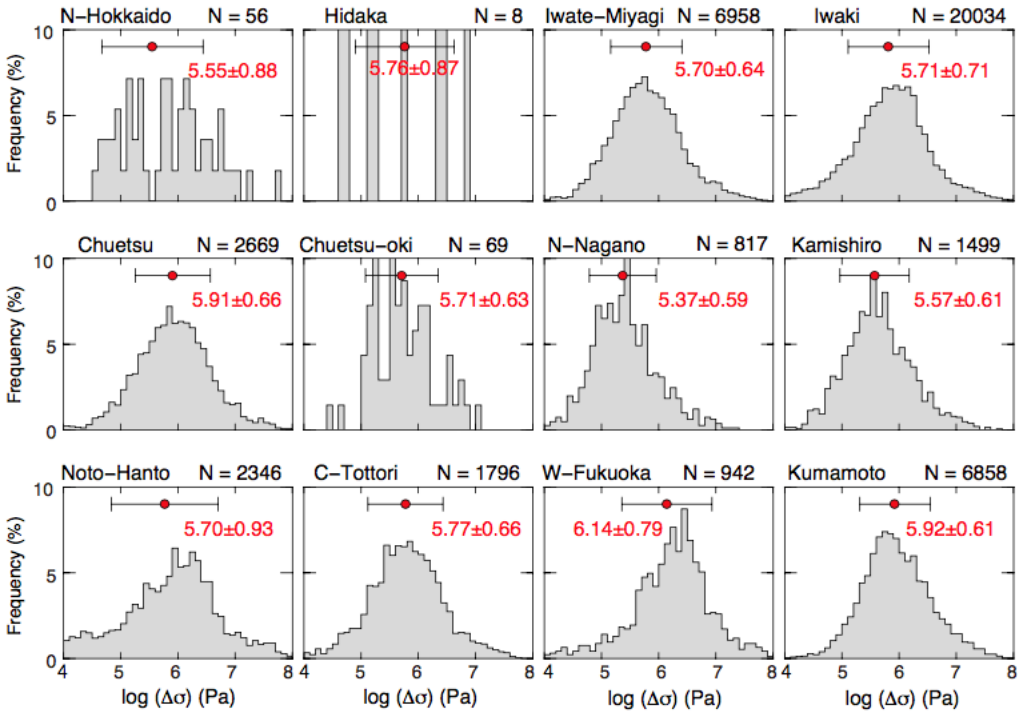

785

786 **Figure 8.** Frequency histograms of Δσ for the 2.0≤M≤3.5 earthquakes in the 12 areas that were
787 identified in Figure 7d. The name of each hypocentral area and the number of analyzed
788 earthquakes are displayed at the top of each panel. The average and standard deviation in each
789 area are shown by a circle with error bars.

790

791

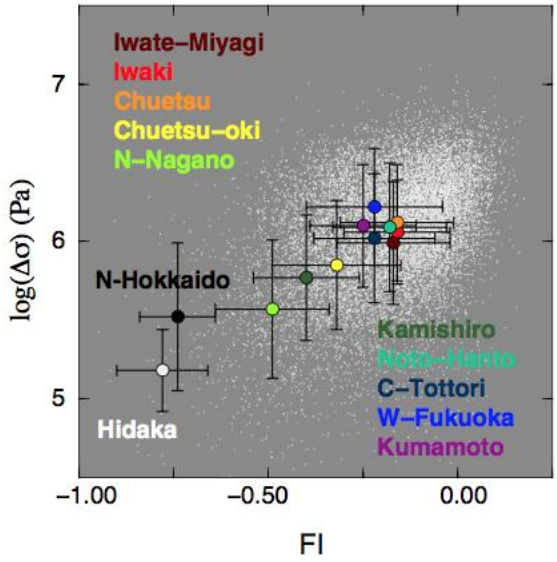

792

793 **Figure 9.** Comparison of the Δσ and FI (gray dots) values for the analyzed 2.0≤M≤2.5
794 earthquakes. The averages and standard deviations of the FI and Δσ values in each of the 12 areas
795 that were identified in Figure 7d are shown by the colored circles with error bars.

796

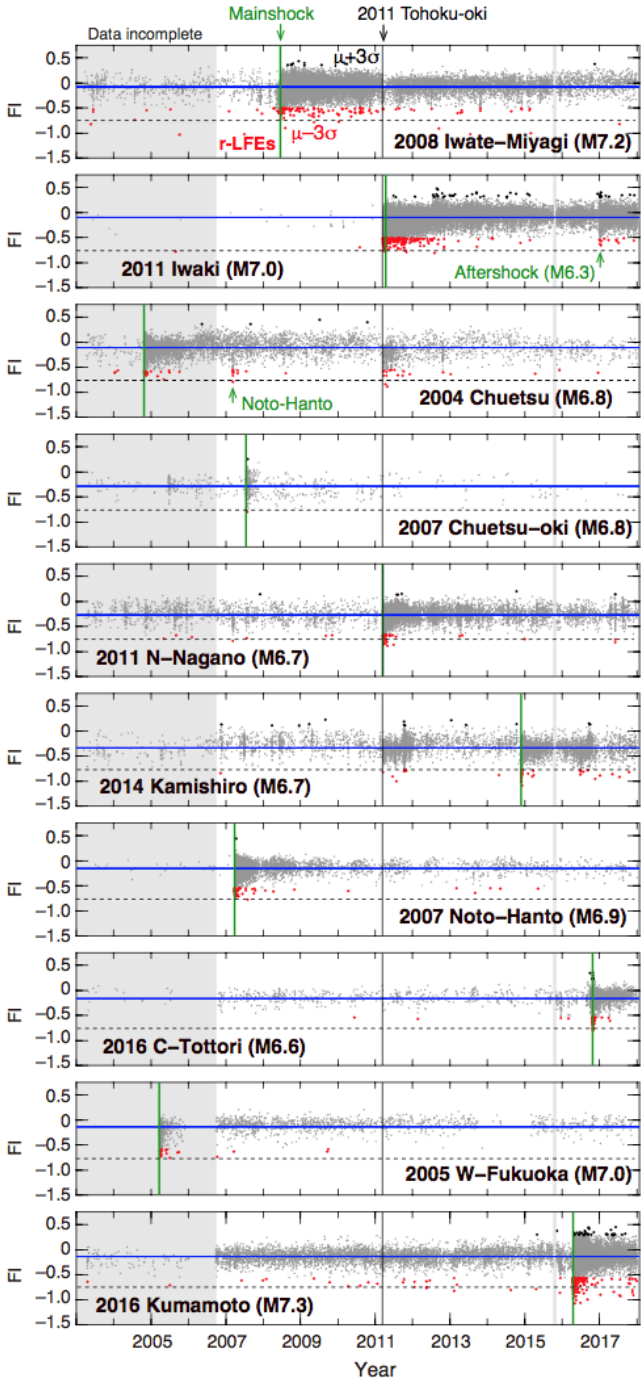

797

798 **Figure 10.** Temporal variations in the FI values (gray dots) for the ten hypocentral areas and the
799 entire analysis period (2003–2017), with the average values (blue lines) shown. The r-LFEs are
800 shown by the red circles. The timing of the mainshock for each sequence and the 2011 Tohoku-
801 oki Earthquake are shown by the green and black vertical lines, respectively. The horizontal
802 dashed lines denote FI = –0.75, which was used to re-define the LFEs in this study. The periods
803 with incomplete data are shown by the gray bands.

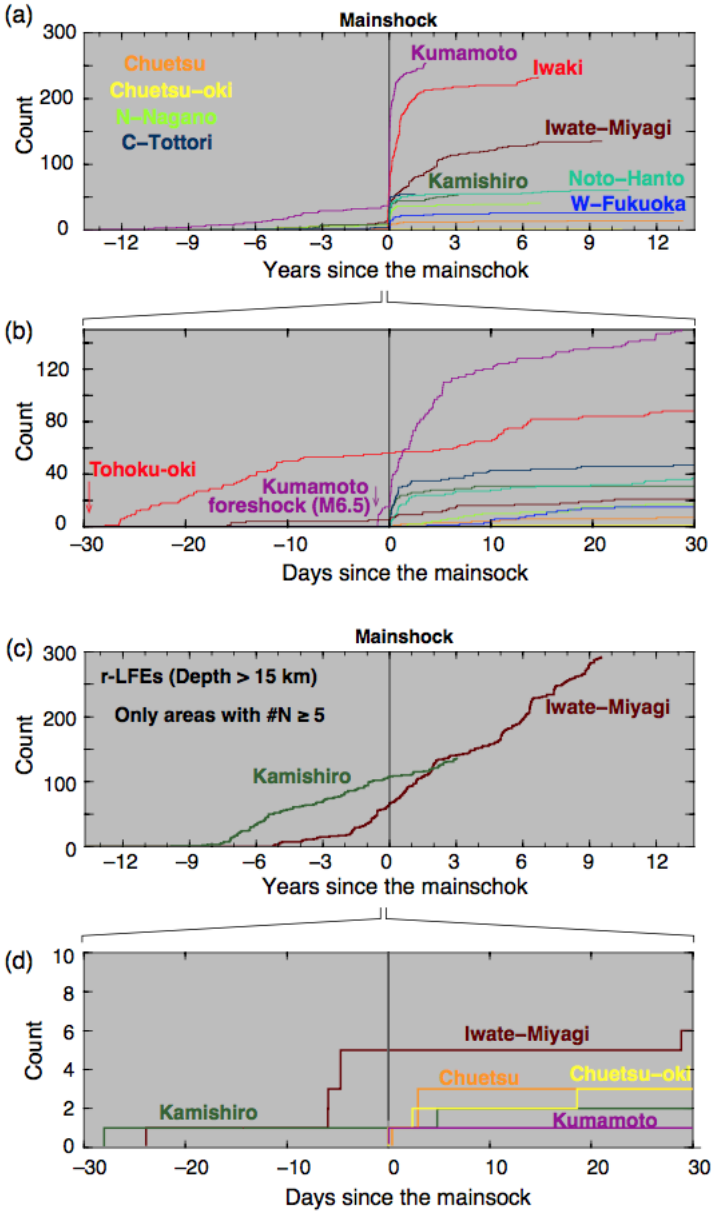

Figure 11. Cumulative counts of the (a,b) shallow (≤15 km depth) r-LFE and (c,d) deep (>15 km depth) LFE activity for the ten hypocentral areas. The LFE activity for the entire analysis period (2003–2017) is shown in (a) and (c), and the short-term LFE activity (30 days before and after the mainshock) is shown in (b) and (d). The colors represent the LFE counts for each sequence.

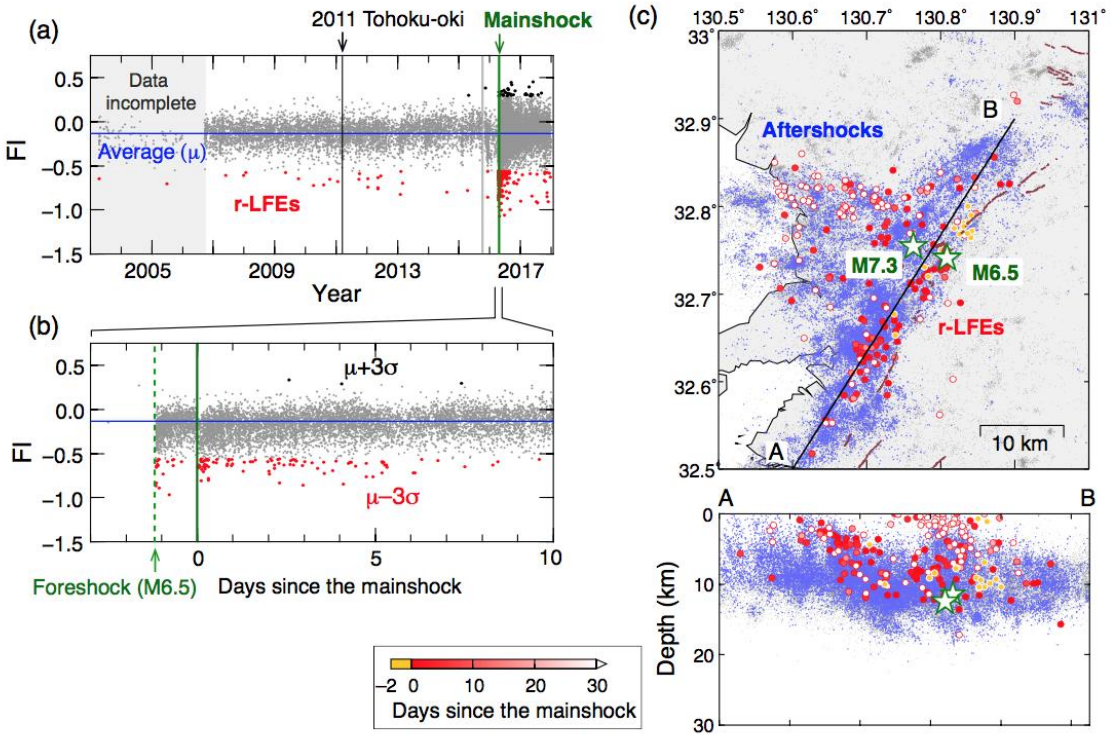

811
812

813 **Figure 12.** (a) Temporal variations in the FI values (gray dots) for the entire period of the
814 Kumamoto sequence, with the average value (blue line) shown. The r-LFEs are shown by the red
815 circles. The timing of the 2011 Tohoku-oki Earthquake and mainshock of the 2016 Kumamoto
816 sequence are shown by the gray and green vertical lines, respectively. The periods with
817 incomplete data are shown by the gray bands. (b) Calculated FI variations from three days before
818 to ten days after the mainshock. The time of the largest foreshock (M6.5) is shown by the green
819 dashed line. (c) Hypocenter distributions of the r-LFEs (large circles) and other earthquakes (blue
820 dots) whose FI values were calculated. The r-LFEs are color-coded with respect to the elapsed
821 time since the mainshock. The bottom panel shows vertical cross section A–B in the map. The
822 hypocenters of the M6.5 foreshock and M7.3 mainshock are indicated by the green stars. The
823 major fault traces are shown by the brown lines.
824

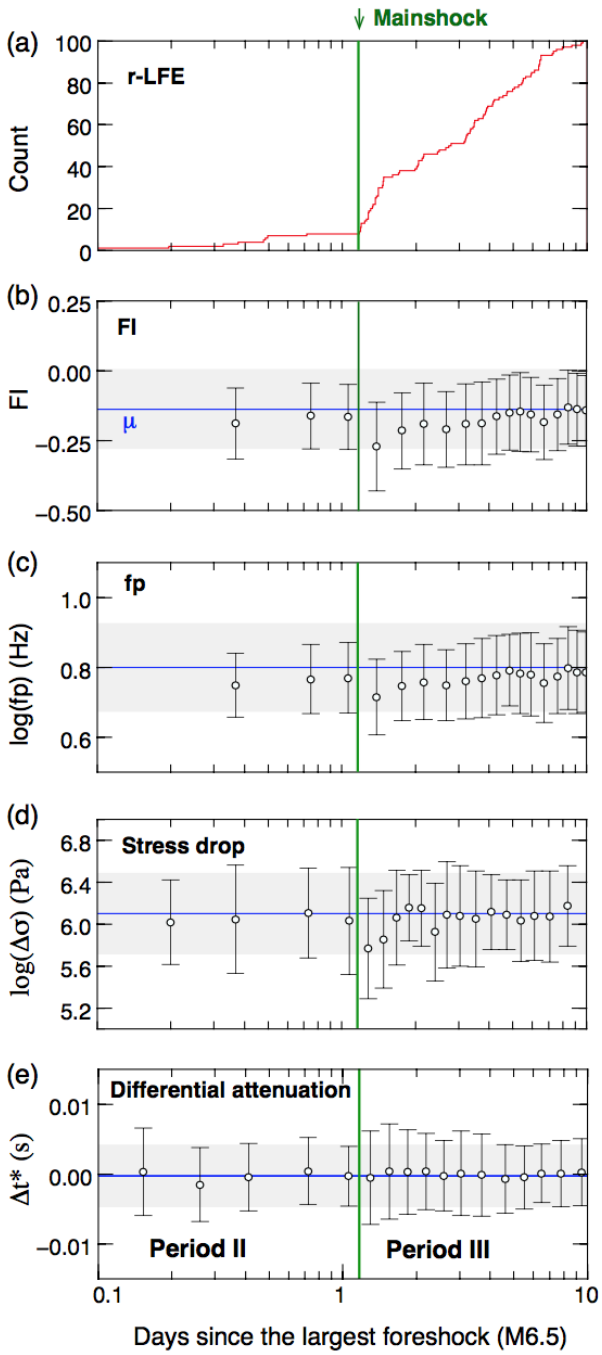

825

826 **Figure 13.** Temporal variations in the (a) number of r-LFEs, (b) FI values, (c) f_p values, (d) $\Delta\sigma$,
827 and (e) differential attenuation (Δt^*) during the 10 days following the M6.5 foreshock. The
828 horizontal blue lines and gray band show the average and its standard deviation of each value for
829 the entire period, respectively. The average value and standard deviation of the FI and f_p values,
830 $\Delta\sigma$, and Δt^* are calculated for every successive 500 earthquakes, 50 earthquakes, and 300
831 earthquakes, respectively.

832

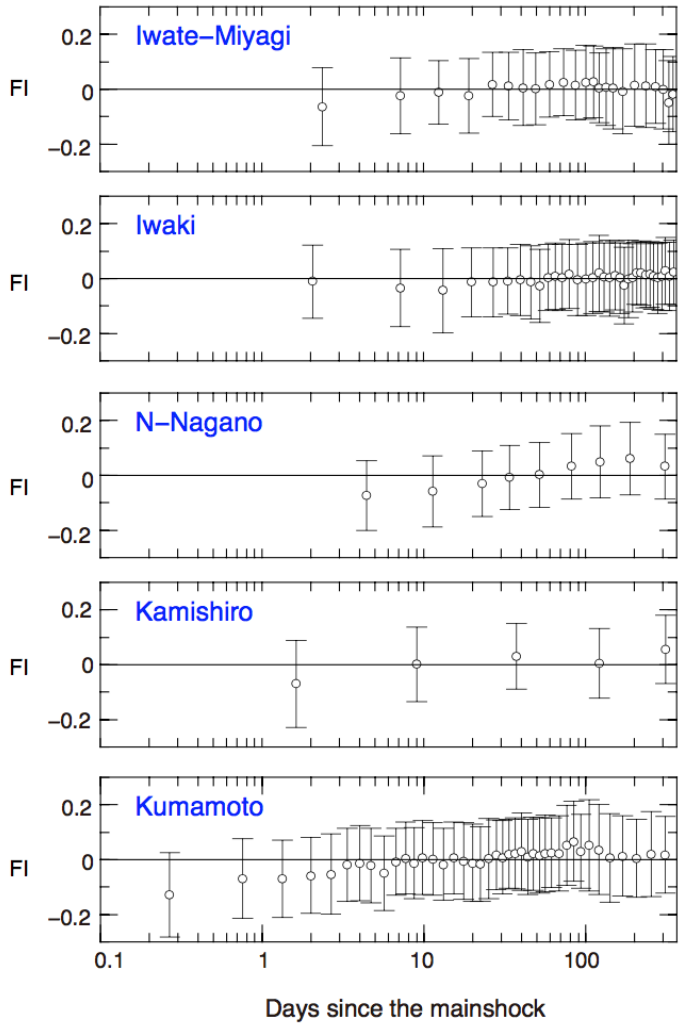

833
834

835 **Figure 14.** Temporal variations in FI for the shallow earthquakes (<15 km depth) in five
836 hypocentral areas where LFEs and r-LFEs are active. The vertical axis is the deviation from the
837 average FI value in each region. The average and standard deviation of the FI values are calculated
838 for every successive 500 earthquakes.

839
840

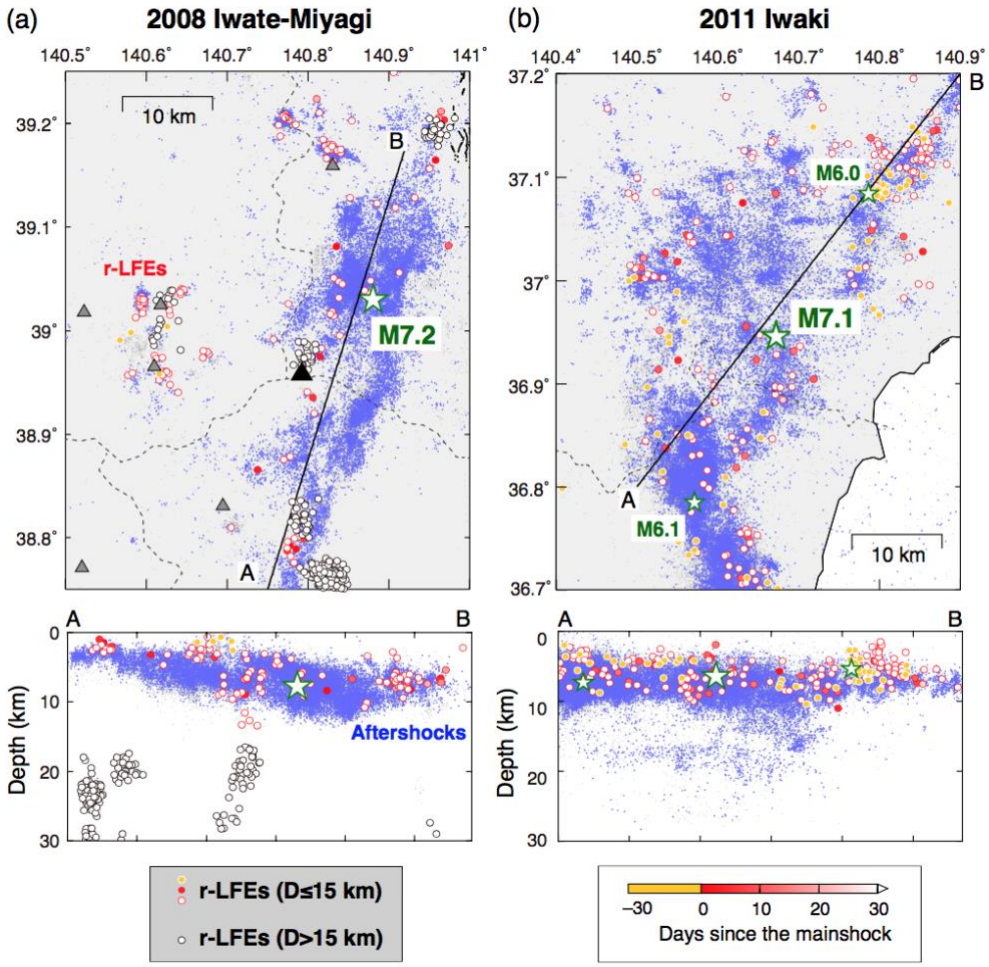

841

842

843 **Figure 15.** Hypocenter distribution of the r-LFEs (large circles) and other earthquakes (blue dots)
844 whose FI values are calculated for the (a) 2008 Iwate-Miyagi and (b) 2011 Iwaki sequences. The
845 r-LFEs are colored with respect to the elapsed time since each mainshock. The A–B vertical cross
846 sections are shown in the bottom panels. The mainshock hypocenters are shown by the large green
847 stars. The hypocenters of two moderate-size foreshocks (M6.0 and M6.1) prior to the 2011 Iwaki
848 sequence are shown by the small green stars. The black and gray triangles denote active and
849 Quaternary volcanoes, respectively.

850